

POLITECNICO DI TORINO

Corso di Laurea Magistrale  
in Ingegneria Aerospaziale

Tesi di Laurea Magistrale

Modeling of orbital and attitude dynamics  
of a satellite controlled via active  
electrostatic charging



**Relatori:**

Prof. Sabrina Corpino  
Dott. Marco Quadrelli

**Candidato:**

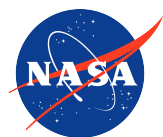
Filippo Corradino

Marzo 2018

This work is licensed under the Creative Commons Attribution 4.0 International License. To view a copy of this license, visit <http://creativecommons.org/licenses/by-nc-nd/4.0/>.







**Jet Propulsion Laboratory**  
California Institute of Technology

This research was carried out at Jet Propulsion Laboratory, California Institute of Technology, during the internship sponsored by JVS RP (JPL Visiting Student Research Program) and NASA.

# Contents

<b>Abstract</b>	<b>3</b>
<b>1 Introduction</b>	<b>5</b>
1.1 Nanosatellites space exploration . . . . .	5
1.2 The E-Glider concept . . . . .	6
1.3 Previous work and objectives . . . . .	6
1.4 Work organization . . . . .	7
<b>2 Electrostatic Flight</b>	<b>9</b>
2.1 Plasma basics . . . . .	9
2.1.1 Plasma modeling . . . . .	11
2.2 Plasma environment . . . . .	12
2.2.1 Overview . . . . .	12
2.2.2 PIC analysis . . . . .	14
2.3 Electrostatic dynamics analysis . . . . .	18
2.3.1 Hovering on the subsolar axis . . . . .	18
2.3.2 Electrostatic orbiting . . . . .	20
2.3.3 Spacecraft-induced effects . . . . .	22
2.4 Spacecraft charging dynamics . . . . .	24
2.4.1 Charge collection in a plasma . . . . .	24
2.4.2 Spherical and cuboid electrodes . . . . .	25
2.4.3 Wire electrodes . . . . .	27
2.4.4 Mass and environments sensitivity analysis . . . . .	29
2.4.5 Challenges and future perspectives . . . . .	30
2.5 Extension to planetary atmospheres: Mars . . . . .	30
2.5.1 Requirements for levitation . . . . .	31
2.5.2 Plasma interaction . . . . .	32
2.5.3 System sizing . . . . .	32
2.5.4 Conclusions . . . . .	34
<b>3 Active Charge Control</b>	<b>36</b>
3.1 Active electrostatic orbit control . . . . .	36
3.1.1 Reduction to 2D problem . . . . .	36
3.1.2 Dynamics and control model . . . . .	37

3.1.3	PID Controller . . . . .	40
3.1.4	Future work . . . . .	41
<b>4</b>	<b>Dynamics Modeling and Simulation</b>	<b>44</b>
4.1	Overview . . . . .	44
4.1.1	Code structure description . . . . .	45
4.2	Reference Frames . . . . .	47
4.2.1	Rotation Matrices . . . . .	48
4.2.2	Heliocentric Frames . . . . .	49
4.2.3	Main Body Centered Frames . . . . .	51
4.2.4	Spacecraft Centered Frames . . . . .	54
4.3	Integrator core . . . . .	55
4.3.1	First cardinal equation . . . . .	56
4.3.2	Second cardinal equation . . . . .	59
4.3.3	Control equations . . . . .	59
4.4	Gravitational forces modeling . . . . .	59
4.4.1	Point-Mass model . . . . .	59
4.4.2	Spherical Harmonics model . . . . .	60
4.4.3	Forces and Torques . . . . .	62
4.5	SRP forces modeling . . . . .	65
4.5.1	Force components on an illuminated surface . . . . .	65
4.5.2	Computation of SRP forces and torques . . . . .	67
4.5.3	Implementation in the code . . . . .	69
4.6	Electrical forces modeling . . . . .	70
4.6.1	Forces and Torques . . . . .	71
4.7	Testing and Future work . . . . .	73
<b>5</b>	<b>Conclusions</b>	<b>75</b>
<b>A1</b>	<b>Quaternions</b>	<b>77</b>
<b>A2</b>	<b>Fast Keplerian Solver</b>	<b>79</b>

# Abstract

The work presented in this thesis was carried out at the Robotics division of NASA JPL, with the main objective of improving and developing mathematical and computational models for the electrostatic flight of nanosatellites. The reference project for the activity was the E-Glider concept, developed by Dr. Marco Quadrelli in the context of the NASA Innovative Advanced Concepts (NIAC) Program.

The large-scale exploration of airless bodies, such as asteroids, moons, and comets, is becoming of great interest, however it is limited by mobility issues both for traditional landers and orbiters.

The E-Glider is an advanced concept for small satellite mobility and propulsion, which relies on the electric fields and the solar wind plasma naturally present around these bodies in order to generate manoeuvring forces and torques.

It does so by extending electrically charged appendages (or electrodes), which allow it to electrostatically levitate above the surface, or control its attitude if differentially charged. It is a mostly propellant-less system, which ideally only requires electric power to re-emit the neutralizing current collected from the plasma.

After an extensive review of the existing literature and the previous work performed by Dr. Quadrelli and its collaborators, three main areas of work for the modeling activity were identified:

- The refinement and expansion of models concerning the E-Glider interaction with the electric environment.
- The definition and validation of an active position/attitude charge control strategy.
- The development of an orbital and attitude dynamics simulator, valid for arbitrary spacecrafts and main bodies, including modeling of gravitational, radiation pressure and electrostatic interaction.

The electrostatic environment analysis highlighted the necessity of PIC simulation data for the plasma environment simulation, which was provided by prof. Joe Wang and William Yu of USC.

With the support of this data, a detailed analysis of the electrical requirements for various mission scenarios was performed, and a study on optimal electrodes geometry was

built upon the results. Thin, long, wire electrodes were found to be the most power-efficient, albeit sometimes requiring very high potentials, the feasibility of whose will have to be carefully evaluated in future analyses, especially from a technological perspective.

The active control study aimed at developing and simulating a position and attitude controller in a simplified 2D model. A PIC controller, based on linearized dynamics, was realized and tested, with excellent results. This result proves the applicability of the E-Glider technology as an attitude control and stationkeeping system.

Finally, a multifield dynamics simulator, **AMOSPy**, was developed in Python, to become in the future a software testbench for E-Glider concepts, and allow the verification of active charge control algorithms, trajectory stabilities, and the calculation of power requirements. It can also easily be applied to study all kinds of other small satellites mission.

Some strong points of this simulator consist in fast, nonsingular gravity models, a very accurate and robust raytracing algorithm to calculate solar radiation pressure effects, and a proximity dynamics model which is valid also for eccentric orbits of the target body (while most standard models are only valid for quasicircular orbits).



# Chapter 1

## Introduction

### 1.1 Nanosatellites space exploration

While a few years ago nanosatellites were mainly thought of as cheap small-scale technology demonstrators or academic didactic instruments, the industry has quickly caught on, and nowadays small satellites of all scales find more and more applications in serious commercial or scientific missions.

Many new companies, such as GomSpace, Planet Labs, Terran Orbital, ISIS now focus on this new sector of the space industry, while also launcher manufacturers develop new, small, platforms aimed at this segment, such as Electron, SS-520, PLD ARION and others.

While commercial Earth-observation and communications payloads are becoming a new norm for nanosatellites, the "new frontier" is represented by interplanetary missions, large-scale space exploration and high-level scientific missions.

For all of these scenarios, there is a need for new, advanced technologies to be developed for these small satellites, especially in three aspects:

- **Propulsion**, an aspect which constitutes both a challenge and an opportunity due to the small sizes and masses available: the constraints are very limiting, however some unusual propulsion systems such as FEEPs or solar sails, which were impractical on larger spacecrafts, can now be employed.
- **Communications**, which is not exceptionally critical while in LEO, but becomes a great concern for deep space missions, especially due to the low power available, the need for complex, directional antennae, and the pointing requirements.
- **Navigation and control**, in particular for autonomous navigation and for accurate pointing, both for communication (see previous point) and especially for complex scientific payloads.

The research on new enabling technologies for mobility and control solutions in nanosatellites is therefore paramount for the successful development of this growing sector of the

space industry.

If properly developed, these technologies could bring about a new season of scientific space exploration with unprecedented possibilities of relatively cheap, large-scale operations.

One such technology could be the E-Glider concept, developed at NASA JPL by Dr. Marco Quadrelli.

## 1.2 The E-Glider concept

The large-scale exploration of airless bodies, such as asteroids, moons, and comets, by means of small satellites, is becoming of great interest; it is however often limited by mobility issues: the lack of an atmosphere, low gravity, and unknown soil properties pose a difficult challenge for many forms of traditional locomotion.

The space environment in proximity of these bodies is electrically charged due to interactions with the solar wind plasma and UV radiation.

The E-Glider is an advanced concept for small satellite mobility and propulsion, which relies on these electric fields and the solar wind plasma naturally present around airless bodies, in order to generate forces and torques useful to its manoeuvring and its mission.

It does so by extending electrically charged appendages (or electrodes), which allow it, for instance, to levitate over the similarly charged surface of an asteroid. By charging differently different electrodes it can also produce torques in order to control its attitude and orientation in space.

The charges are maintained by continuous ion or electron emission (as necessary) from the spacecraft, by means of small particle guns or similar devices, in order to cancel out the neutralizing influx of charges from the surrounding plasma. The power expenditure needed to accomplish this could virtually be the whole "cost" of the E-Glider propulsion system, thus enabling it to perform long duration missions without the issue of propellant exhaustion.

Another key advantage of the E-Glider is its ability to operate in a controllable manner very close to asteroid surfaces, in an environment which is challenging both for traditional spacecrafts (due to the very low gravity stable orbits are hard to achieve) and landers, which rely on friction properties of the soil which cannot be determined *a priori*.

## 1.3 Previous work and objectives

A large body of work was already available on the E-Glider concept [21][22], and in particular several models of the spacecraft orbital and electrostatic dynamics had been realized. The objective of this study was to build upon these existing studies and

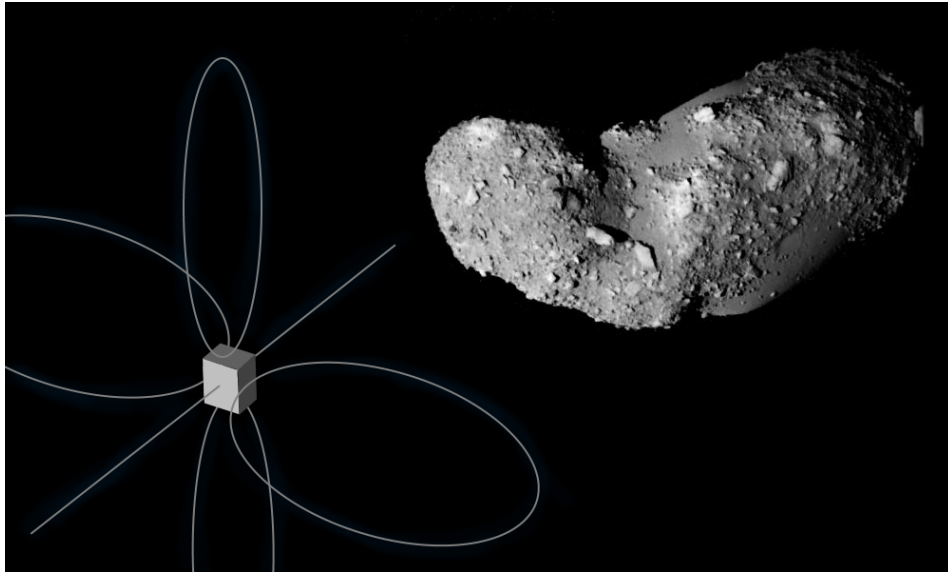


Figure 1.1: Artist rendering of an E-Glider spacecraft in the proximity of Itokawa, sporting thin wire electrodes (four looped and two linear)

improve the available models.

Three main areas of work can be identified:

- The refinement and expansion of models concerning the plasma physics and electrostatics of the E-Glider interaction with the electric environment.
- The definition of an active position/attitude charge control strategy and its validation through simulation.
- The development of a complete orbital and attitude dynamics simulator, valid for arbitrary spacecraft geometries and main body properties, including modeling of gravitational, radiation pressure and electrostatic interaction.

The electrostatic environment analysis highlighted the necessity of PIC (Particle-In-Cell) simulation data for the plasma environment simulation, some of which was kindly provided by prof. Joe Wang and William Yu of USC (University of Southern California).

## 1.4 Work organization

In the following three chapters the work performed in each one of these three areas of work will be presented.

- In Chapter 2 the electric environment around an airless body will be analyzed, also through the results obtained by the PIC analyses. An analysis of the electrical requirements for various mission scenarios will follow, and the obtained results will

lead into a study on optimal electrodes geometry. Finally, a possible adaptation of the E-Glider technology to planetary atmospheres will be considered.

- Chapter 3 will be concerned with the definition of the active position/attitude charge control strategy and its validation.
- Chapter 4 will present the developed multifield dynamics simulator, **AMOSPy**, starting from the high-level structure and then delving into the details of the dynamics models and the various forces modeling (gravitational, SRP and electrostatic). An overview of the testing campaign and the simulator performance will conclude this section.

A few appendices also provide further insights into some technical mathematical aspects.

# Chapter 2

## Electrostatic Flight

### 2.1 Plasma basics

Before delving into the details of the electrostatic Spacecraft/Asteroid/Plasma interactions, a short foreword on some basic concepts of plasma physics is presented.

Plasma is defined as a quasineutral ionized gas; it is therefore a gas whose particles are at least to some extent ionized, thus exhibit net electric charges, however over large scales the net charge tends to zero.

Particles in a plasma are unbounded, like they would be in a gas, however besides the kinetic interactions which are present in a gas, they also interact with each other and with the environment through the Maxwell equations, generating and responding to electromagnetic fields and electrical currents.

An important parameter in plasma physics is the **Debye length**, which is the characteristic length of the plasma and depends on particle density and temperature:

$$\lambda_D = \sqrt{\frac{\varepsilon_0 k_B q_e^2}{\sum \frac{n_x}{T_x}}} \quad (2.1)$$

$\varepsilon_0$  and  $k_B$  are respectively the vacuum permittivity and the Boltzmann's constant,  $q_e$  is the elementary charge,  $n_x$  and  $T_x$  are the number density and temperature of species  $x$ . The Debye length indicates the spatial scale of electric fields decay in a plasma. Charges in a plasma are free to move, and in the presence of an external electric field, positive charges will be attracted "downstream" along the field lines, while negative charges will be attracted "upstream" in the opposite direction<sup>1</sup>. This creates localized space charges

---

<sup>1</sup>It is important to note that this is only a large-scale and time-averaged effect, due to an average deflection of trajectories. The kinetic energy of particles in a plasma far outweighs the potential energy introduced by an electric field, thus the single particle will still freely buzz around, its motion only minimally (but on the whole, not insignificantly) perturbed. Electric fields in a plasma work much like pressure gradients in a standard gas

which induce a shielding electric field, opposite to the external one.

Suppose, for instance, that a positively charged spherical electrode, of radius  $R$  and voltage  $V_0$ , is immersed in a plasma. While in a vacuum its electric field would decay with an inverse square law [2.2a], in a plasma it would decay exponentially [2.2b]. The space near the electrode would be depleted of cations and attract anions, creating a sort of virtual electrode which shields the bulk of the plasma from the field of the original electrode. This charged volume is called the plasma sheath or **Debye sheath**.

$$V(r) = V_0 \left( \frac{r}{R} \right)^2 \quad \text{in a vacuum} \quad (2.2a)$$

$$V(r) = V_0 e^{-\frac{r-R}{\lambda_D}} \quad \text{in a plasma} \quad (2.2b)$$

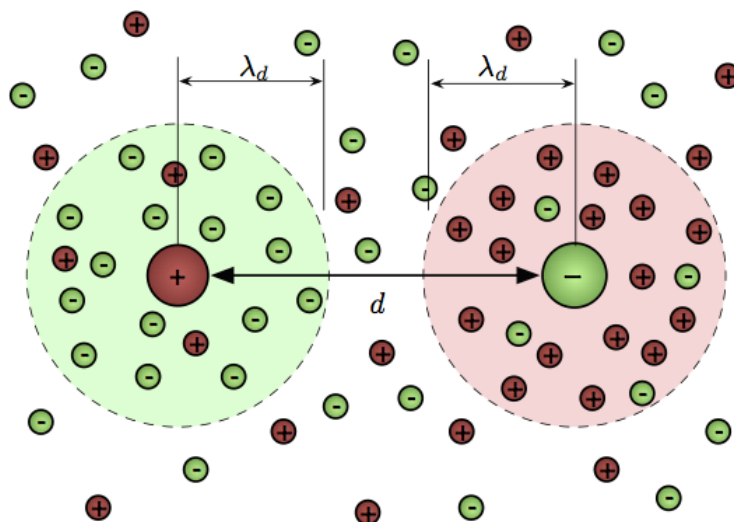


Figure 2.1: Simplified representation of Debye shielding of two electrodes

Generally speaking, the electric field of the electrode can be neglected beyond a few Debye lengths.

This may not be true when the electrode potential is very high, in which case the Debye sheath expands due to saturation effects and may transition into what is known as a Child-Langmuir sheath [12].

The Debye shielding can be advantageous, at least in the scope of this work, since it increases the capacitance of the electrode (thus reducing the required potential for a given charge) and "hides" the electrode from the bulk of the plasma (possibly reducing collection currents).

### 2.1.1 Plasma modeling

Plasmas can assume incredibly different characteristics and typical behaviours depending on composition, ionization, thermodynamical properties, magnetization etc. Since it can exist in a huge array of conditions, it sometimes seems improper to talk about it as if it were a single state of matter. Different kinds of plasmas can act as differently as a gas and a liquid, or more.

For this and other reasons, there is not one single way to approach plasma modeling, however one could identify two general strategies, which can then be attuned and adapted to a wide array of specific cases [10].

#### Analytical modeling

Analytical modeling of plasmas usually combines the Maxwell equations with some kind of kinetic or continuum theory, depending on the plasma and the scales considered.

Most "classical" plasmas are weakly coupled, that is the long-range interactions due to distributed space charges dominate wrt the short-range particle-particle interaction. This behaviour is reminiscent, in a sense, of the gravitational force, which is usually very weak between small, near objects, but very significant over large scales.

This usually holds if  $\Lambda \sim n\lambda_D^3 \gg 1$ , that is if a volume with dimensions in the order of the Debye length contains a great number of particles.  $\Lambda$  is called the plasma parameter.

A widely applied equation which is valid for weakly coupled plasmas and is based on a kinetic theory is the **Vlasov equation**:

$$\frac{\partial f}{\partial t} + \mathbf{v} \cdot \nabla \cdot f - q \left( \mathbf{E} + \frac{\mathbf{v}}{c} \times \mathbf{B} \right) \quad (2.3)$$

The Vlasov equation describes the evolution of the particle distribution function  $f(\mathbf{x}, \mathbf{v}, t)$ , which indicates the probability density for finding a particle in a certain point in the phase space at time  $t$ .

If complemented with the Maxwell equations, the new system is called the Vlasov-Maxwell equations, and it can be used effectively to model most standard plasmas, often with some simplifying assumptions (e.g. one can derive the MHD equations from these). It can be said that the Vlasov-Maxwell equations are the de-facto starting point for most analytical plasma modeling theories [10].

The general downside of the analytical approach is the daunting task of solving the equations for non elementary cases, even by employing numerical methods.

Unfortunately the plasma modeling considered in this work belongs to the group of problems which are not easily approachable with an analytical approach, if one doesn't want to commit gross simplifications [27].

## PIC simulation

The alternative to analytical modeling is direct simulation using some sort of discretization scheme, much like CFD for aerodynamics.

The PIC approach (Particle In Cell) is one of these methods. It is based on the direct simulation of motion of "macroparticles", representing often many millions of particles at once, and their relative interaction.

Computing the electrical interaction between each two pair of macroparticles would lead to a complexity  $\mathcal{O}(N^2)$ , with  $N$  being the number of macroparticles, which is usually impractical even with the current processing power ( $N$  is often in the millions).

In the PIC approach, instead, at each computational step the macroparticles charge and currents are "spread" on an underlying discrete mesh (from which the name "particle in a cell"); the electromagnetic field is then computed over this mesh from the Maxwell equations and reinterpolated on the various macroparticles. This allows to lower the complexity to  $\mathcal{O}(N + M)$  where  $M$  is the number of nodes in the mesh [3].

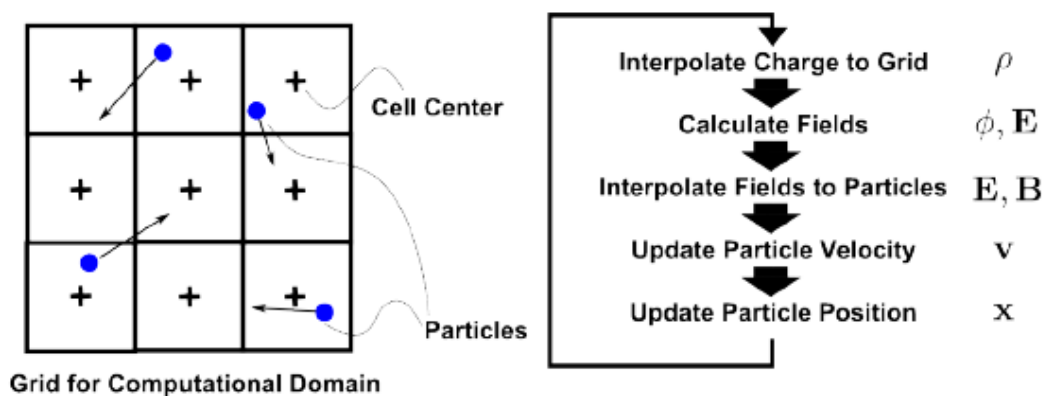


Figure 2.2: Simplified PIC method scheme

## 2.2 Plasma environment

### 2.2.1 Overview

Most asteroids (and, more generally, airless bodies) can be modeled as high-resistivity spheroidal bodies immersed in the solar wind plasma stream. The side facing the incoming solar wind is also illuminated by the Sun.

Both the solar wind and the solar radiation interact with the surface to generate or exchange charges. Due to the high resistivity, neutralizing currents within the celestial body are limited, and local charges accumulated on the surface are mostly maintained; thus, high potential gradients can be present on the asteroid surface [13] [16].

The main actors in charge extraction and transfer are [24]:



- **Ions** usually positively charge surfaces upon impact, with the following mechanisms according to their energy:
  - $T < 10^5$  eV - low energy ions tend to extract electrons from the surface and depart as neutral atoms (charge exchange);
  - $T > 10^5$  eV - high energy ions also induce secondary electron emission, that is more than one electron is ejected from the surface for each impacting ion, effectively enhancing the charging effect.
- **Electrons** usually negatively charge surfaces upon impact, with the following mechanisms according to their energy:
  - $T < 10^2$  eV - low energy electrons are simply absorbed by the surface;
  - $T > 10^2$  eV - high energy electrons also induce secondary electron emission, which reduces the effectiveness of the charging mechanism; it can be said that the surface gains a positive "electrical albedo", since the phenomenon is analogous to a partial reflection of the incoming electrons.
- **Photons** in high energy bands (UV, X-ray or above) extract electrons from the surface by the photoelectric mechanism.

The average properties of the solar wind and solar illumination at a distance  $d$  [AU] from the Sun, calculated assuming a polytropic expansion, is summarized in the table below [13]:

Parameter		Value	
SW ion density	$n_{i0}$	$5 \cdot 10^6/d^2$	$\#/m^3$
SW electron density	$n_{e0}$	$5 \cdot 10^6/d^2$	$\#/m^3$
SW ion temperature	$T_{i0}$	$10/d^{2/3}$	eV
SW electron temperature	$T_{e0}$	$15/d^{2/3}$	eV
SW drift speed @1 AU	$v_s$	$350/d^2$	km/s
SW ion Mach number @1 AU	$M_i$	10	
Solar constant	$P_s$	$1350/d^2$	W
Photoelectron current	$j_{p0}$	$5 \cdot 10^{-6}/d^2$	A/m <sup>2</sup>

At the representative distance of 1 AU the solar wind is therefore composed of ions (mainly protons) and electrons, with a density of 5 particles per  $cm^3$  and temperatures around  $10 \div 15$  eV, while the basic photoelectron emission current is  $5 \mu A/m^2$ .

The solar wind at 1 AU is mesosonic: the ions are supersonic, i.e. their drift velocity is much greater than their thermal velocity, while the electrons are subsonic, since their lower mass and greater mobility mean they have much higher thermal velocities.

For this reason, the ions streaming past the asteroid form a significant wake behind it,

in which only the mobile electrons can penetrate (Figure 2.3).

Only electrons can therefore impinge on the dark side of the body, which negatively charges until the local electric field is strong enough to reflect all incoming electrons. At equilibrium, the potential on the dark side can thus reach negative values of tens to several hundreds of volts (Figure 2.4) [13] [16].

On the sunlit side, both ions and electrons strike the surface in almost equal proportion. Actually slightly more electrons are collected, again due to their higher mobility in the plasma.

However, photoelectron emission due to the UV radiation from the Sun can significantly influence the equilibrium potential in this region. The emitted electrons cause the surface to accumulate positive charges, until its potential is high enough to impair the emission itself, that is when the emitted photoelectron energy is not high enough to escape the local potential well.

The equilibrium voltage on the sunlit side (neglecting the solar wind effect) will therefore be in the order of the photoelectron thermal voltage, i.e. a few volts.

This differential charging of the sunlit and dark emispheres generates appreciable electric fields in proximity of the surface, and especially in the terminator zones, where its intensity can reach tens of V/m.

### 2.2.2 PIC analysis

A PIC simulation of the plasma environment around an asteroid was performed by William Yu and prof. Joe Wang at USC [27]. The body considered is a 28 m diameter sphere at 1 AU from the Sun. These preliminary results confirm many of the theoretical hypotheses presented above.

The species density distribution (Figure 2.3) in particular shows very clearly the presence of a marked and well defined ion wake.

The solar wind electrons present a slight wake as well, consistent with the negative potential of the dark side. The general rarefaction in proximity of the asteroid surface can be attributed to the overall negative net charge acquired by the body.

Finally, the photoelectrons show a typical diffusion pattern from the sunlit side, and their density rapidly decays to zero with increasing heights.

While the species densities of course determine the whole plasma environment and electrostatic fields, *per se* they only come into play in the E-Glider model when calculating current collection and power expenditure. The electrostatic potential, on the other hand, directly influences the spacecraft dynamics, and it is therefore perhaps the most important result of the simulations.

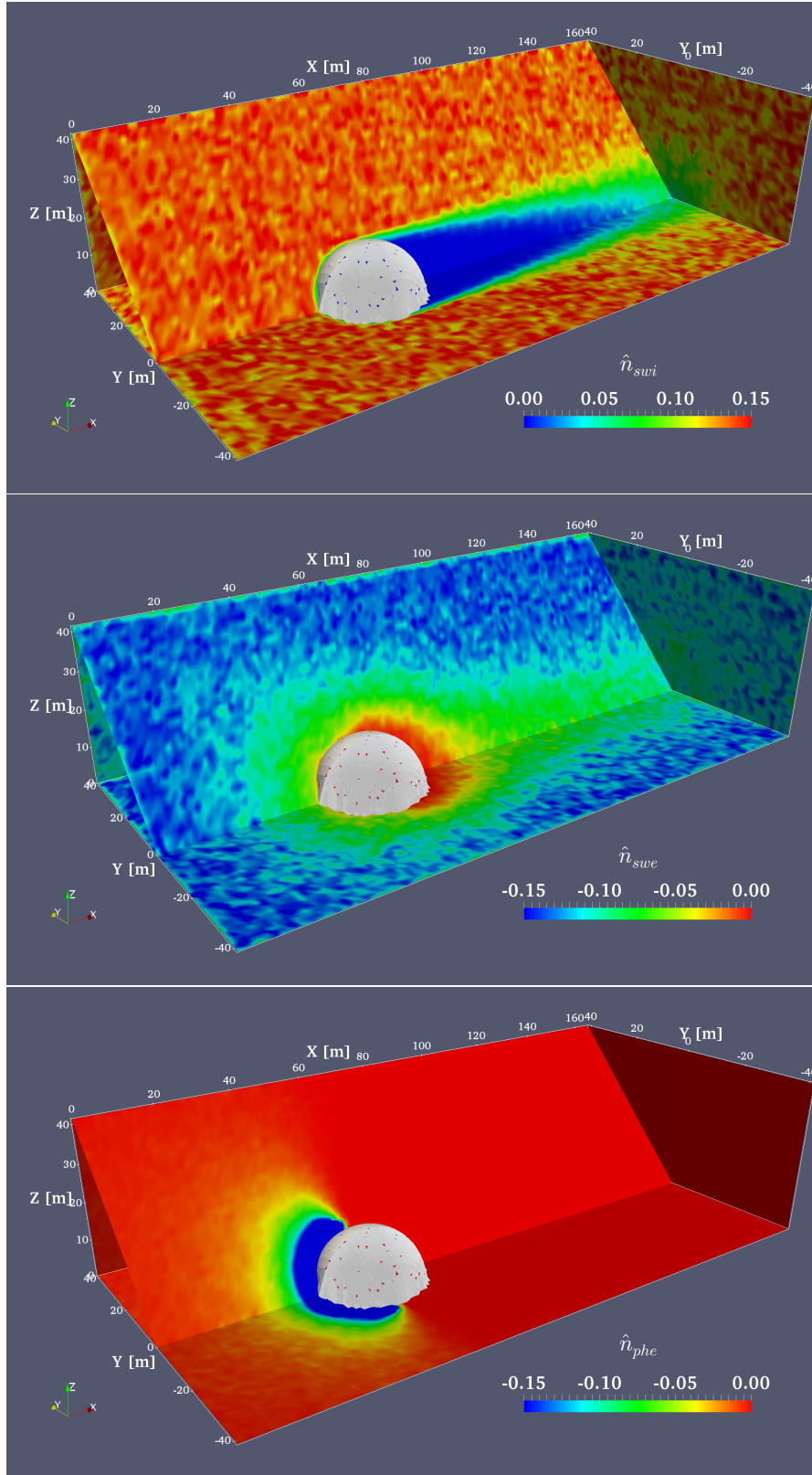


Figure 2.3: Plasma species density from a PIC simulation.

From top to bottom: solar wind ions, solar wind electrons and photoelectrons

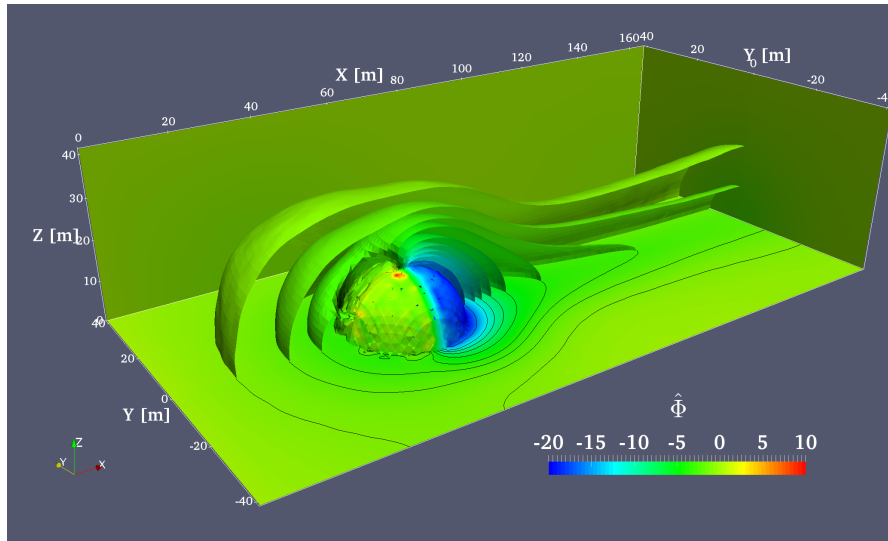


Figure 2.4: Electrostatic potential

As shown in Figure 2.4, the near-surface field resembles that of a dipole, which is consistent with the differential charging phenomenon, while the far field decays radially (except in the wake region). The surface potential is in the range of  $-20$  V on the dark side and slightly negative on the sunlit side. This relatively low and negative potential on the sunlit side indicates that, at least for this size of asteroid, the increased solar wind electron flux is sufficient to offset the positive charge generation caused by the photoelectrons.

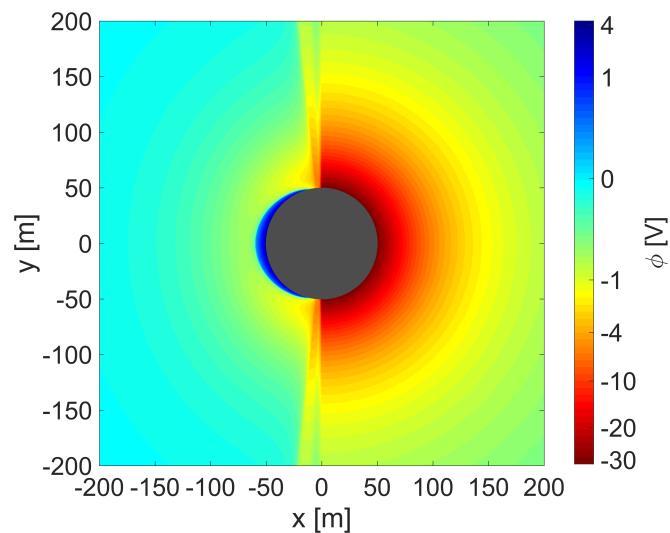


Figure 2.5: Obsolete electrostatic potential calculated with Nitter model

The potential profile obtained from the simulation also shows that the Nitter model implemented in the past [19] [11] does not provide accurate estimates, especially for

small asteroids, being derived from an infinite planar surface 1D model.

The main drawbacks of this model are the inability to correctly capture the wake and its underestimation of the radial decay (Figure 2.5). Both inaccuracies lead to an excessively optimistic and non-conservative estimate of the electric fields.

The electrostatic field intensity, of which the PIC derived data is shown in Figure 2.6, offers virtually the same data as the potential, but in a more easily readable form.

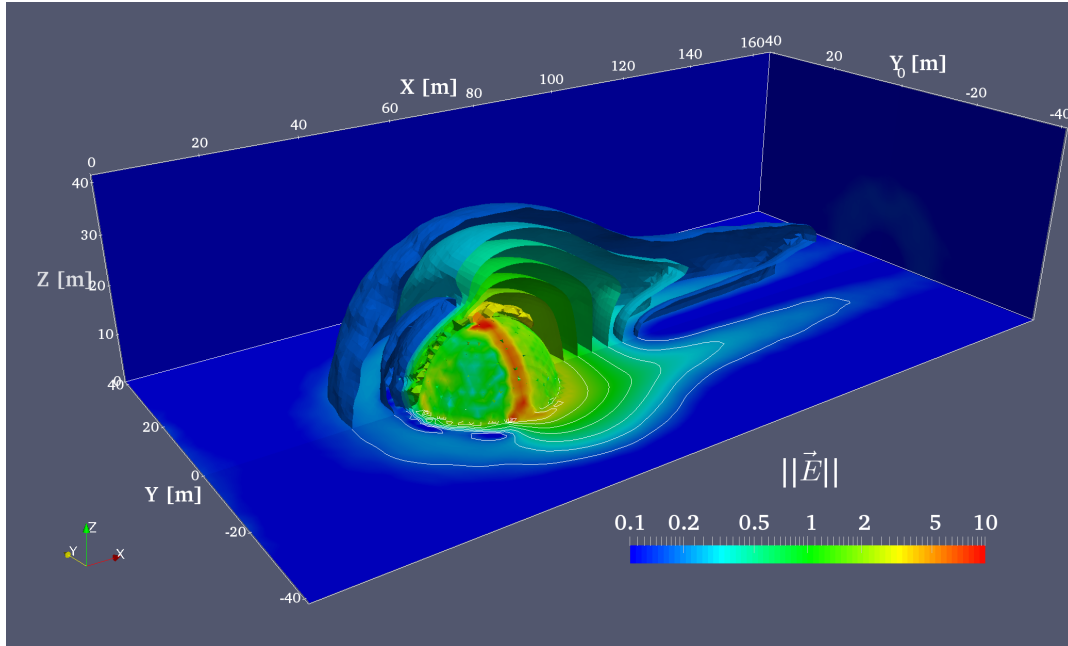


Figure 2.6: Electrostatic field magnitude

It is evident that the highest values are found at low altitude over the terminator, as expected. Also, higher field strength is found over the dark side rather than the sunlit side, again consistently with the more significant potentials in that region.

This is not optimal for the E-Glider operation, since the regions of interest are the sunlit ones, and a weaker electric field there implies the necessity for higher spacecraft charges, potentials and consequently power consumption.

It must also be noted that these PIC results might not be easily scalable to different asteroid geometries and dimensions, since while some phenomena (e.g. the ion wake) are scale-dependent, others depend on scale-invariant quantities such as the Debye length of the plasma.

They are however extremely useful in confirming and defining with good confidence the actual qualitative electrostatic environment around an airless body.

## 2.3 Electrostatic dynamics analysis

### 2.3.1 Hovering on the subsolar axis

This first PIC data provided by William Yu and prof. Joe Wang can also be used to revisit the equilibrium analysis performed in the past by Shota Kikuchi [21] with the Nitter model.

The objective is to find equilibrium points for hovering operations along the Sun-asteroid axis and perhaps discuss their stability and spacecraft charge requirements, at least qualitatively.

The main forces at play are:

- Asteroid gravitational force
- Asteroid/plasma electrostatic force
- Solar radiation pressure
- Apparent forces in the non-inertial Hill frame

Of these, the apparent forces are several orders of magnitude smaller than the others, and introduce periodic motions with long characteristic times of approximately 1 yr. They could be thus safely neglected for a first approximation analysis such as the one presented here.

While the relative terms were nevertheless included in the equations used for the simulation scripts, they will be left out in the following presentation for the sake of brevity and clarity.

It is assumed, due to the symmetry of the problem, that all external fields acting on the spacecraft can be expressed as a function  $F(x, r)$  of the coordinate along the subsolar axis ( $x$ ) with origin at the asteroid center, and a radial coordinate ( $r$ ) perpendicular to said axis.

On the subsolar ( $x$ ) axis, it can also be assumed that for any external field  $F$  its radial component  $F_r$  must be null.

The equilibrium to translation along the axis can therefore be written as:

$$g_x + \frac{Q}{m}E_x + \frac{A}{m}p_x = 0 \quad (2.4)$$

Where  $\mathbf{g}$  represents the gravitational acceleration,  $\mathbf{E}$  the electric field and  $\mathbf{p}$  the solar radiation pressure vector<sup>2</sup>.  $\frac{Q}{m}$  and  $\frac{A}{m}$  are respectively the charge-to-mass and surface-to-mass ratios of the spacecraft.

For the surface-to-mass ratio a tentative value of  $0.1 \text{ m}^2/\text{kg}$  was assumed.  $0.01 \text{ m}^2/\text{kg}$  would be characteristic of cubesat-like spacecrafts, but this higher value provides a more

---

<sup>2</sup>The SRP effect is obviously only considered over the sunlit side of the asteroid.

conservative estimate considering the effect of lightweight and large (albeit thin) electrodes.

An asteroid uniform density of  $2200 \text{ kg/m}^3$  was also assumed to compute the gravitational acceleration.

Solving [2.4] for  $Q/m$  one can calculate the required charge-to-mass ratio needed for hovering at any given height.

The results obtained from the PIC analysis are presented in Figure 2.7 below.

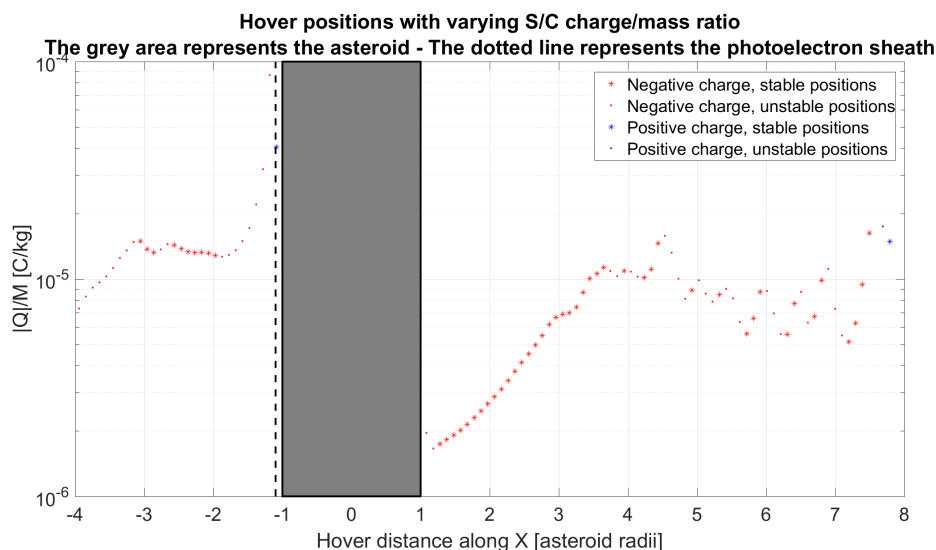


Figure 2.7: Hovering conditions along the subsolar axis. Red asterisks indicate stable positions with negative spacecraft charge

Two important conclusions can be drawn from this analysis.

Firstly, virtually all equilibrium conditions are met with a negative spacecraft charge, except in the nominal (1 Debye length) photoelectron sheath, i.e. below 1.5 m over the surface. This is actually convenient, since a negatively charged spacecraft collects ion currents, which typically turn out to be less intense than electron currents (due to effects related to ion inertia and lower density).

Secondly, there are some stable equilibrium points over the sunlit side (which are the most interesting ones from a mission perspective), i.e. assuming that the charge is kept constant, the spacecraft would not experience drift either towards or away from the asteroid. This may relax some requirements for the charge control system to be employed.

The maximum charge to mass ratio required for levitation over the sunlit region seems to be in the order of  $10^{-5} \text{ C/kg}$ , which is a reasonably achievable value, while still needing very high electrode potentials, but especially at great heights this is not as high as the values calculated in previous analyses [21].

It seems that hovering at altitudes in the order of  $\approx 10^1 \div 10^2$  m would be possible, assuming that voltage and power issues are properly addressed.

### 2.3.2 Electrostatic orbiting

Another option for E-Glider operations is to adopt electrostatic orbiting trajectories rather than performing station-keeping in hover. These trajectories exploit the electrostatic forces to cancel out the  $x$ -axis force components, while radial components are opposed by a centrifugal component introduced with a tangential spacecraft velocity. It is the same principle used for passive terminator orbits.

This approach eliminates the constraint of operating along the subsolar axis, and could allow to exploit areas of more intense electric fields in order to reduce the spacecraft charge needed.

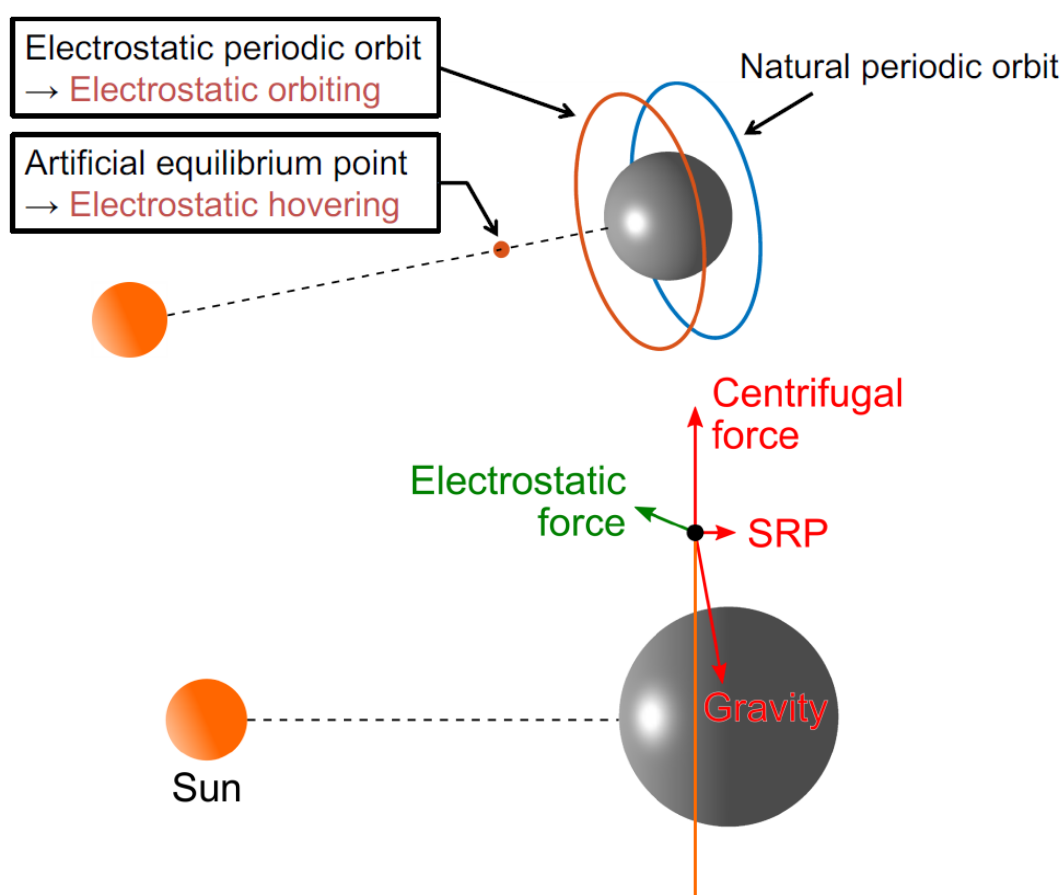


Figure 2.8: Illustration of subsolar hovering and both passive and active terminator orbiting trajectories (above); Electrostatic orbiting forces diagram (below) - courtesy of Shota Kikuchi.



Even though the axial force is not required to be null along the entirety of an electrostatic orbit, if the apparent forces due to the Hill frame are neglected, in at least one point along the trajectory the axial force must be null (due to the intermediate value theorem). Equation [2.4] is therefore still valid for this analysis, with the only difference that the domain can be extended to  $r \neq 0$ . The results are shown in the graphs in Figure 2.9:

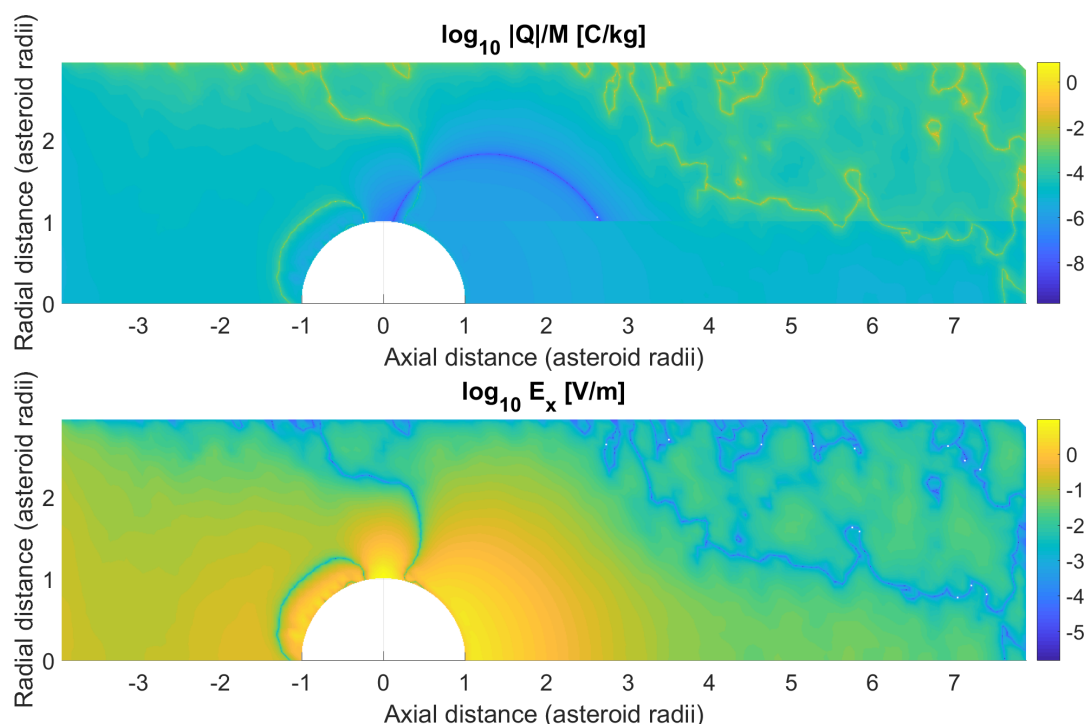


Figure 2.9: Charge-to-mass ratio required for orbiting (above) and axial electric field (below) in the  $x - r$  plane

Apparently few regions over the sunlit area allow for charge-to-mass ratios smaller than the ones needed for hovering.

The terminator region is one of these, as expected, being the one with the strongest electric fields. In the same region one can also find the neutral charge equilibrium for terminator orbits, which is however quite a bit offset towards the dark side (visible as a dark blue arc in the upper half of Figure 2.9).

A moderate spacecraft charge would therefore allow to "push" the passive terminator orbit towards the sunlit side and greatly increase the coverage of illuminated areas on the surface (albeit still at low illumination angles).

A few pockets of strong electric fields and relatively low required charge can be found very near the surface closer to the subsolar point, however operations in these areas might be tricky, due to the proximity of both unfavourable low-field, high-charge requirement

boundaries and of the asteroid surface, which especially for irregular asteroids might impair this kind of low altitude operation or cause strong field irregularities.

Electrostatic orbiting is therefore mainly feasible in the terminator region, with a slight reduction in the required spacecraft charge compared to hovering.

### 2.3.3 Spacecraft-induced effects

The analysis until now has neglected the effect that the spacecraft would have on the surrounding plasma. This is a valid approximation assuming that the sheath surrounding the spacecraft is thin enough. However the high charge-to-mass ratios required imply very high spacecraft potentials, and consequently the plasma sheath (be it ionic or electronic) could significantly expand [12] (see also section 2.1).

This is due to the fact that the spacecraft sheath would be in the current saturation regime. This means that the sheath would contain only one kind of electrical species (the other being completely reflected little after the border), and it would need to expand far enough to collect sufficient current (and therefore maintain sufficient space charge inside it) to counteract the strong electric field generated by the spacecraft.

Let's suppose that a highly charged spacecraft is in the proximity of an asteroid. Should its plasma sheath extend significantly, it could reach the surface, effectively merging with the surface photoelectron sheath.

This interaction, as well as the deflection and disturbances in the solar wind flow already caused by the spacecraft, could modify the particle flows enough to significantly alter the surface charging state of the asteroid, and perhaps modify the conditions required for hovering or orbiting.

This influence, if present, could be compared to the "ground effect" phenomenon that aircrafts experience when their wings are close to the ground (e.g. in landing) and the airflow gets modified significantly.

Preliminary calculations indicated sheaths engorgement even up to hundreds of meters, according to some models. This would have certainly rendered obsolete the previous analysis, so William Yu and Dr. Wang kindly performed new analyses specially aimed at studying the effect of a highly charged spacecraft on the plasma environment.

Apart from a new plasma wake, however, the growth of the spacecraft sheath was found to be modest, and the Debye length could still be used as a reference scale length for it (Figure 2.10). Furthermore, after removing the self-electric field generated by the spacecraft, it was found that the asteroid-generated field was only very slightly perturbed if compared to the one without the biased spacecraft influence.

Overall, this constitutes very good news: the capacitance of the spacecraft is not hindered by an expanded sheath, and the first analysis is still valid (at least for the terminator orbiting scenario, in which the spacecraft ion wake does not interact with the asteroid directly)

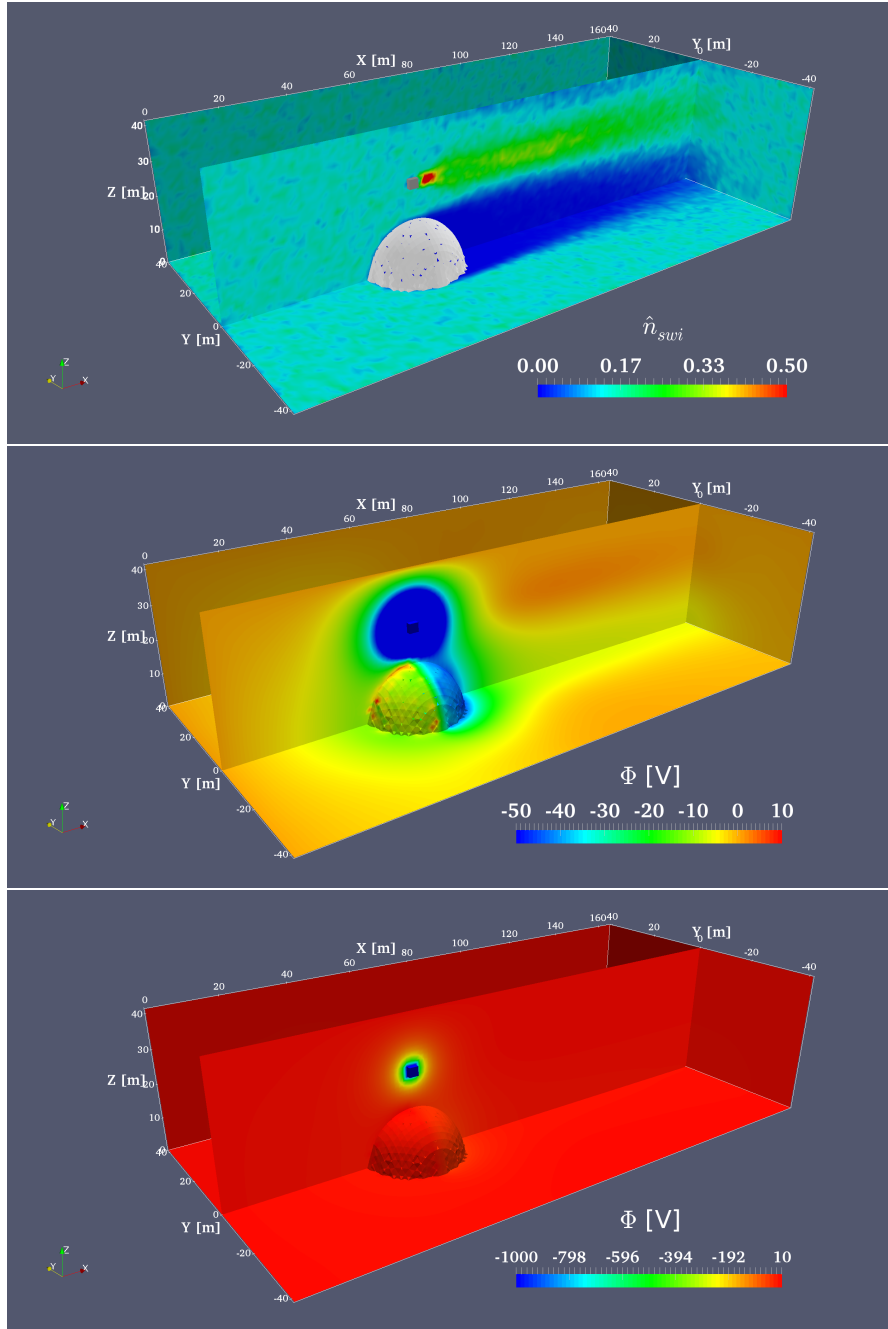


Figure 2.10: PIC simulations with orbiting spacecraft biased to 1 kV. From top to bottom: solar wind ions (with new wake), and two differently scaled versions of the potential; the plasma sheath is large but not more than a few Debye lengths

## 2.4 Spacecraft charging dynamics

### 2.4.1 Charge collection in a plasma

Any electrically biased object immersed in a plasma will be subject to a current from the plasma which tends to bring it to the equilibrium potential (typically slightly negative wrt. the plasma bulk potential).

Since the E-Glider must maintain and control its charge state, these return currents must be precisely re-emitted, by means of electron or ion guns. Since the emitted charges must have at least sufficient energy to escape the potential well of the spacecraft, a good indicator of the power needed for charge-keeping is the product of collected current and spacecraft voltage.

A range of current collection analyses were performed to study this effect, assuming different electrode geometries and plasma conditions.

All these analyses are decoupled from the previous ones concerning the actual plasma environment around the asteroid, for simplicity's sake; different conditions (such as species densities and temperatures) can be set, but the plasma is from now on supposed to be uniform, and the charge-to-mass ratio is the only spacecraft parameter input used.

Since voltage is dependent on charge by means of the capacitance, and the capacitance in a plasma depends on the local sheath (a thin sheath boosts the capacitance), and again the local sheath depends on the electrode voltage, an iterative process is usually required in order to find the correct electrode voltage:

$$\begin{cases} C = C(R, \lambda_D) = C(R, V) \\ V = V(Q, C) \end{cases} \quad \begin{matrix} (2.5a) \\ (2.5b) \end{matrix}$$

The iteration used generally started from an assumed capacitance in a vacuum (thus neglecting the sheath enhancement factor) to obtain an initial conservative estimate of the bias voltage  $V_0$ . Then equations [2.5] were looped, calculating  $C$  from  $V$  and vice-versa, until convergence, measured with a default tolerance on the voltage residuals.

Some useful parameters for these analyses are the adimensional potential  $X$  and the thermal current  $J_{th}$ :

$$X \doteq V/T \quad (2.6)$$

$$J_{thx} = n_x e \sqrt{\frac{eT_x}{2\pi m_x}} \quad (2.7)$$

$V$  is the potential,  $T$  is the plasma temperature in eV.

$n_x$ ,  $T_x$  and  $m_x$  are respectively particle density, temperature and mass for the species  $x$ .

Generally speaking there are two main regimes of current collection in a plasma:

- **Sheath limited** regime is valid when the sheath thickness is low compared to the electrode dimension. This is for instance the case for the analyzed spherical or cuboid electrodes. In this regime basically all particles which enter the Debye sheath are then captured by the electrode, therefore the current density is mostly limited to the thermal current incident on the sheath surface (since outside the sheath there are no fields which can attract other particles). The net collected current is therefore limited by the sheath dimensions.
- **Orbit motion limited** or OML is valid when the electrode dimensions are far smaller than the Debye length. This is often the case for thin wire electrodes. In this regime, only a small fraction of the particles which enter the sheath are collected, while most are simply deflected without getting close enough to the electrode to be captured (following a trajectory resembling an hyperbolic orbit). In this case the current is therefore limited by the electrode dimensions, and by the distance of minimum approach of each particle trajectory, hence the name.

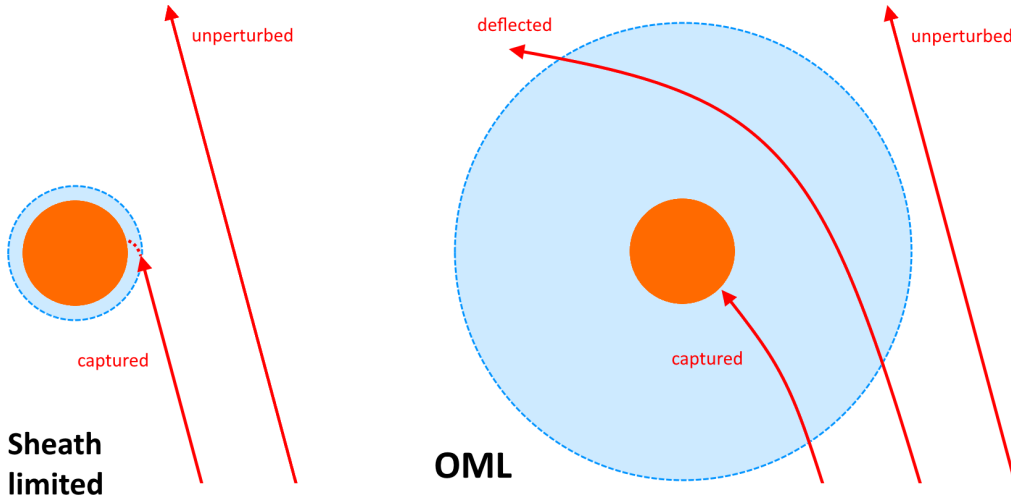


Figure 2.11: Comparison of trajectories in the SL and OML current collection regimes.

### 2.4.2 Spherical and cuboid electrodes

The analysis for current collection on spherical and cuboid electrodes was performed for electron sheaths only, i.e. for positive spacecraft potentials, according to the models developed by I. Bell [2].

According to Bell, the current density to a positively biased spherical electrode in a plasma is given by:

$$J_S = J_{the}(1 + \gamma_a) \left( 1.0 + 0.83 \left( \frac{\lambda_D}{R} \right)^{\frac{2}{3}} \sqrt{X} \right)^2 \quad (2.8)$$

$\gamma_a$  is a corrective factor accounting for plasma flow current collection enhancement effects, and it is  $\approx 3$ , while  $\lambda_D$  and  $R$  are respectively the local Debye length and electrode radius.

The current density to a cuboid electrode is instead:

$$J_C = J_{the}(1 + \gamma_a) \left( 1 + \lambda_D \frac{a + b + c}{(ab + bc + ca)} \pi^{5/4} \sqrt{\frac{2}{9}} X^{3/4} \right) \quad (2.9)$$

In which  $a$ ,  $b$ ,  $c$  are the cuboid dimensions.

The general advantage of these kind of electrodes is their high capacitance, which allows for reduced potentials. Low potentials are very desirable, because as it can be inferred from the formulae above, they imply lower currents, thus lower power and less secondary parasitic effects such as sputtering, secondary electron and radiation emissions, and heating.

On the other hand, a big drawback of these electrodes is their high surface area, and therefore their high current collection and often prohibitive power consumption. Mitigation options for this issue exist and consist in using a relatively high number of electrodes with a certain optimal dimension. Spreading the charge over more than one electrode reduces the required potential, while increasing the collection area. Overall, however, the power surface density decreases faster than the increase in area and this is why using more electrodes can turn out to be convenient.

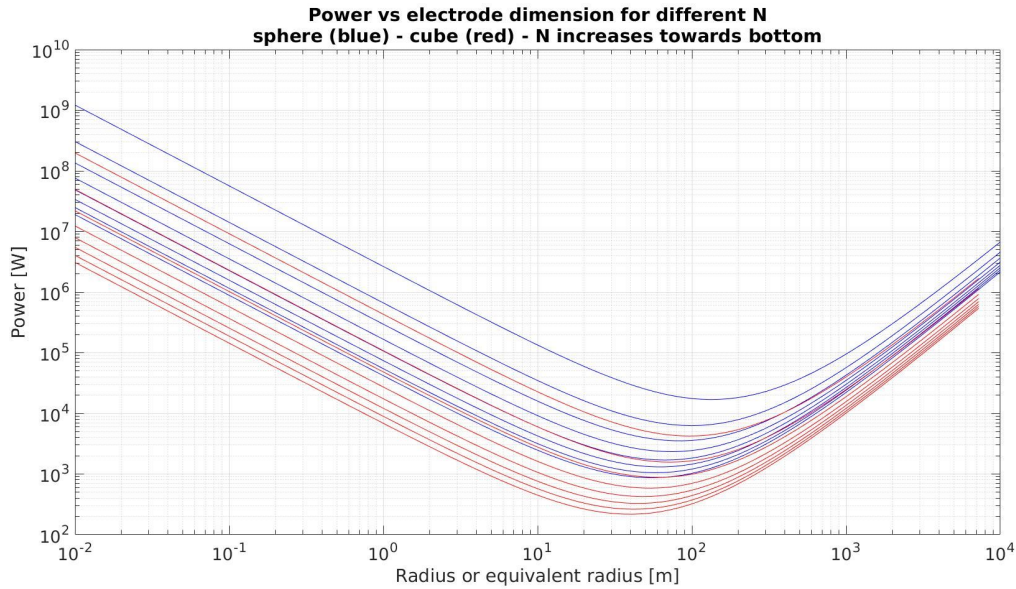


Figure 2.12: Power required for hovering at a hypothetical charge of  $3 \cdot 10^{-5}$  C for different electrode dimensions and number. Blue lines: spherical electrodes, red lines: cubic electrodes.

Limitations of this analysis include neglecting the inter-electrode influence (which modifies the overall capacitance) as well as the electrodes mass, which was assumed to be negligible wrt the spacecraft mass (this is true if ultra-thin electrostatically inflatable electrodes are used).

Even with optimal conditions the required power for hovering with these kind of electrodes turns out to be in the order of  $10^2 \div 10^4$  W (Figure 2.12), which is still impractical. However, the milder conditions presented by ionic sheaths, and eventual ground effect phenomena could reduce these values enough to make them a feasible option.

### 2.4.3 Wire electrodes

The analysis for current collection on wire electrodes was performed for both ionic and electronic sheaths, i.e. for both positive and negative spacecraft potentials.

Since the electrodes are assumed to be lines or loops of thin wire, the characteristic dimensions of which are much smaller than one Debye length, the OML (Orbital Motion Limited) current collection theory was adopted. This theory has very good accuracy in this thick-sheath regime [4][8].

The currents to a wire electrode (respectively, ion current and electron current) are:

$$J_W = J_{thi} \frac{2}{\sqrt{\pi}} \sqrt{Ti + F - V} \quad (2.10)$$

$$J_W = J_{the} \frac{2}{\sqrt{\pi}} \sqrt{1 + X} \quad (2.11)$$

These electrodes have opposite pros and cons wrt the spherical/cuboid ones: while they have very little surface area (and therefore current collection), their capacitance is relatively low, and they require higher potentials.

The reduction in power consumption is however proportionally much more significant (more than 3 orders of magnitude decrease in power with the same charge and plasma conditions), and assuming that the necessary potentials can be achieved, this can easily bring the system power budget in the nanosatellite range of feasibility.

While this analysis still did not include inter-electrode influence, the variability of the spacecraft mass due to the electrodes was considered.

Figure 2.13 shows the electrode potential and spacecraft power needed for hovering over the subsolar point, assuming a basic spacecraft mass of 3 kg (without electrodes). The required power levels are very easily achievable, being mostly below 1 W for a wide range of electrode dimensions.

The limiting factor would probably be, as anticipated, the required potential. This is mostly influenced by the electrode length, and more than 50 m of equivalent length



would be needed if the potential is to be kept below 100 kV. This would be bulky but not unachievable, especially if multiple loop electrodes<sup>3</sup> are arranged all around the spacecraft (e.g. 8 loops 2 m in diameter could be enough).

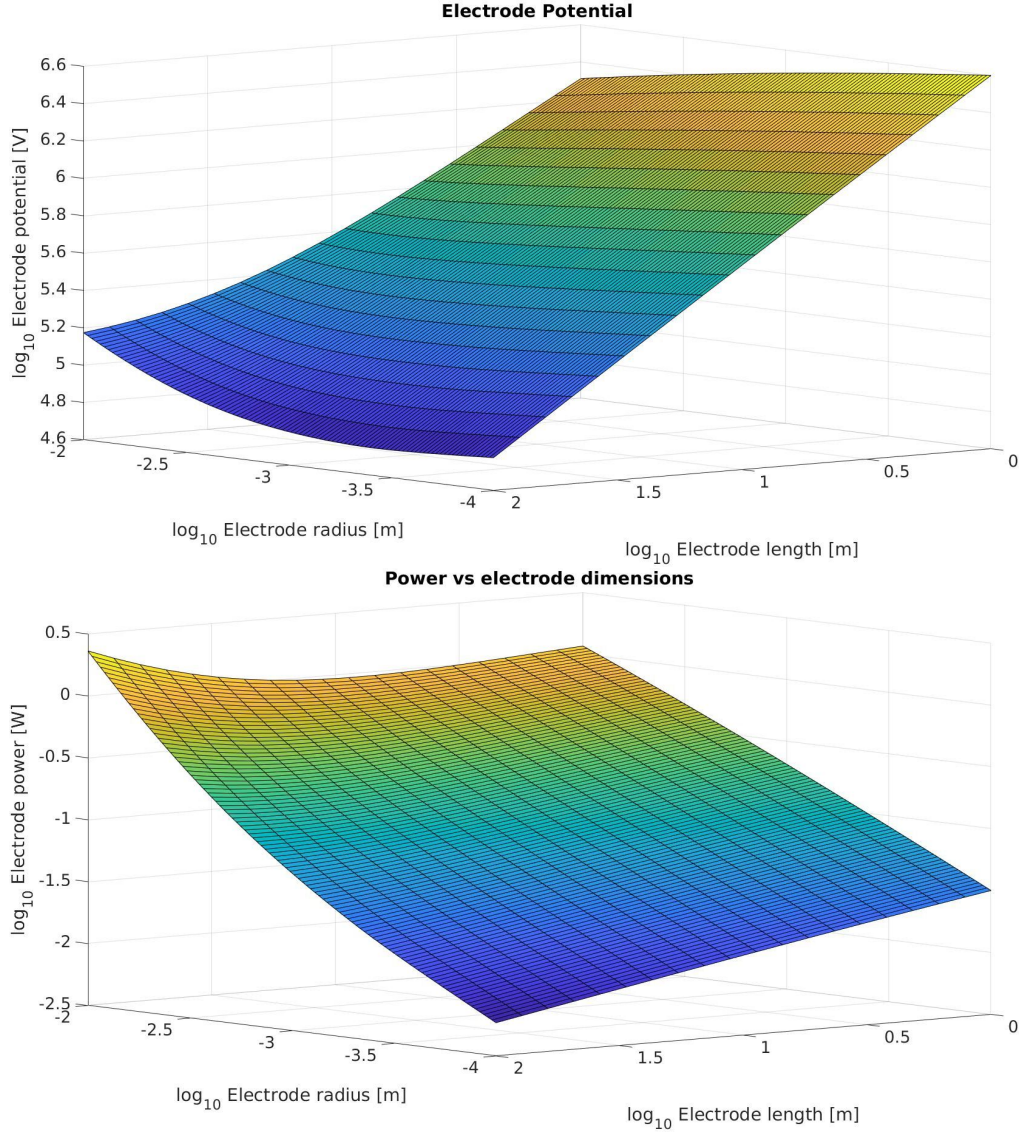


Figure 2.13: Electrode potential (above) and power consumption (below) in hover with varying wire radius and length

<sup>3</sup>Loop electrodes behave almost exactly as a straight electrode with length equivalent to their circumference.



### 2.4.4 Mass and environments sensitivity analysis

Other auxiliary analyses that were performed include a mass sensitivity analysis and a comparison among operations in different plasma environments in the Solar System, both for a selected plausible geometry based on wire electrodes. Some of the results are summed up by the plots here below.

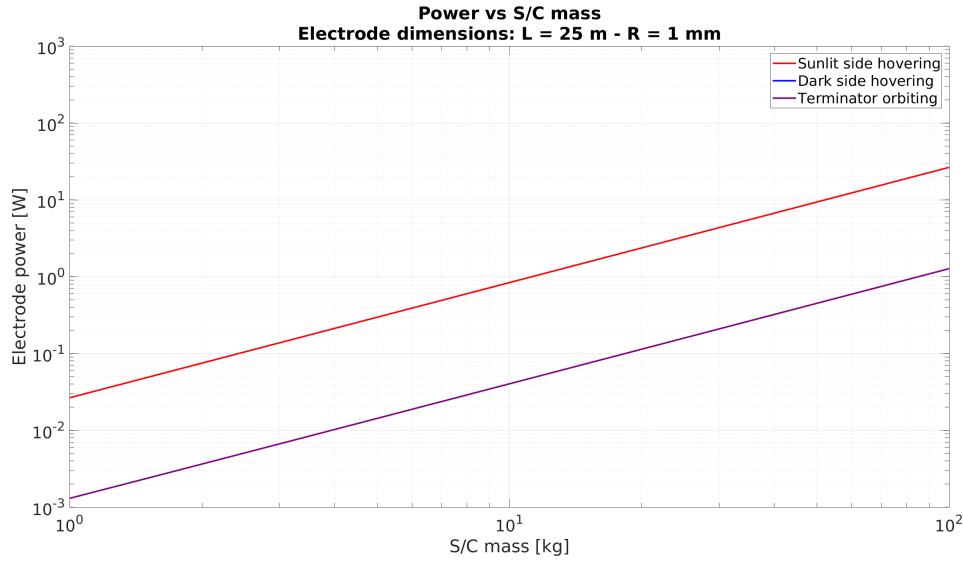


Figure 2.14: Power consumption vs mass in various conditions

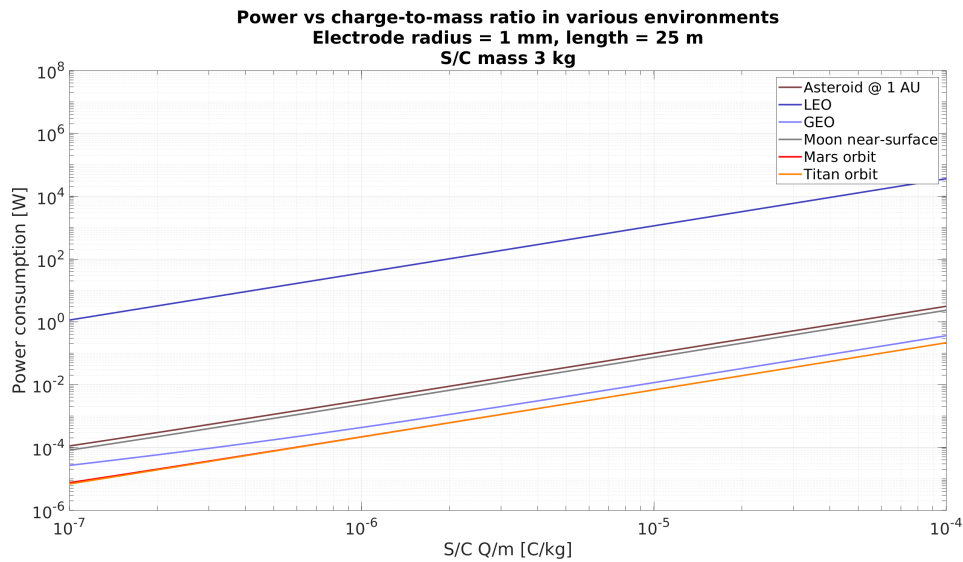


Figure 2.15: Power consumption in various Solar System plasma environments

As already noted, wire electrodes are able to provide lift with very reduced power consumption, well below 1 W/kg, which is totally achievable with current smallsat technology (state-of-the-art CubeSats can already achieve 10 W/kg peaks).

This kind of electrostatic propulsion could allow increased mobility and mission opportunities not only around asteroids, but also moons and perhaps planets, as long as the plasma densities aren't too high (e.g. not in LEO, as shown by the last plot).

Levitation in the wake of an airless body can be accomplished with virtually no power expenditure, even in close proximity to the surface. It must be noted, however, that this also offers penalties for optical payloads operating in the visible spectrum and most importantly for power generation (solar power would be unavailable).

### 2.4.5 Challenges and future perspectives

There are still some issues to be considered in later stages of the system analysis, concerning the high electrode potentials. Having ions impinge on a thin wire with energies of several keV or even MeV produces a wide array of secondary effects:

- Secondary electron emission
- X-ray and other hard radiation emission
- Cathode/Anode sputtering and erosion
- Cathode/Anode heating
- Thermionic emission

Of these effects, only heating and thermionic emission were estimated in this first analysis, and were both found to be negligible for virtually all the possible operating conditions. Most of the overtemperature due to heating would not be more than a few 10s of Kelvins, and definitely not enough to induce significant thermionic emission, especially for negative spacecraft potentials.

The other phenomena could however be more severe and possibly degrade the system performance if not accounted for.

Apart from this, to date, thin wire electrodes seem to constitute a very promising option, especially in terms of power consumption, enabling the E-Glider concept to be applied to self-sufficient solar electric powered nanosatellites.

## 2.5 Extension to planetary atmospheres: Mars

While the E-Glider concept has been developed as a mobility enhancement technology for missions around airless bodies, one of its early inspirations actually stemmed from an atmospheric application: some spiders on Earth, in fact, use electrified silk threads

to lift themselves into the air, exploiting the natural planetary electric field.

It seems therefore interesting to at least evaluate the feasibility of a similar application for the E-Glider in a planetary atmosphere.

Mars was chosen for a simple case study, and this section illustrates the requirements for electrostatic levitation of an E-Glider "blimp" in the martian atmosphere, at an altitude of 10 km.

## 2.5.1 Requirements for levitation

### Atmospheric electric field

The martian atmosphere, much like that of the Earth, acts as a giant spherical capacitor, with the planetary surface and the ionosphere acting as the two electrodes.

On the Earth the charge of this planetary capacitor is maintained by the powerful effect of thunderstorms, which act as generators, while calm weather regions are permeated by a very small leakage current. The equilibrium field is in the order of 100 V/m.

Dust storms on Mars are thought to act in a similar way, however they are much more seasonal (while on Earth, at any given time, in the order of 1000 storms are active). Therefore while in the calm season the martian atmospheric field is very small ( $\approx 0.15$  V/m), during the storm season it can reach values of 475 V/m in fairweather regions (directed away from the surface) [7].

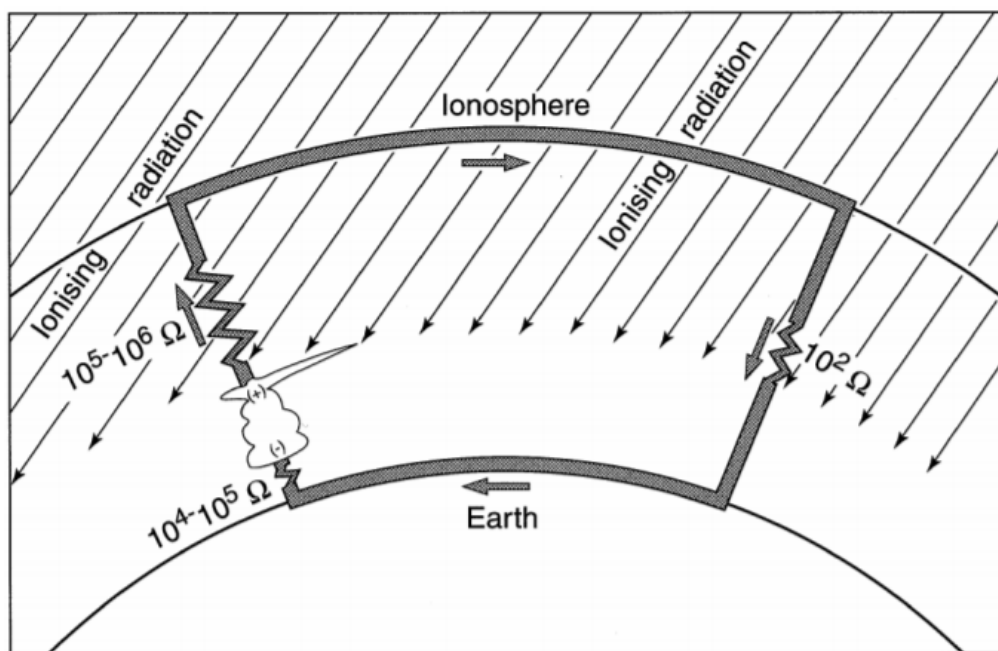


Figure 2.16: Atmospheric electric circuit of the Earth.

### Charge/mass ratio

The gravitational acceleration at 10 km on Mars is  $\approx 3.69 \text{ m/s}^2$ .

Assuming this best-case scenario of  $E_z \approx 475 \text{ V/m}$  the minimum charge/mass ratio required for levitation can be calculated as follows:

$$QE = gM \implies \frac{Q}{M} = \frac{g}{E} \approx +7.8 \text{ mC/kg} \quad (2.12)$$

## 2.5.2 Plasma interaction

### Atmospheric environment at 10 km

According to NASA's [Mars Atmosphere Model](#) [25], the martian atmosphere at 10 km has the following thermodynamic properties:

$$\begin{aligned} p &\approx 284 \text{ Pa} \approx 2.13 \text{ torr} \\ T &\approx 228 \text{ K} \approx 0.02 \text{ eV} \end{aligned}$$

The most abundant ionic species are [17]:

- positive hydronium hydrates ( $\text{H}_3\text{O}^+(\text{H}_2\text{O})_n$ )
- negative carbonate ion hydrates ( $\text{CO}_3^-(\text{H}_2\text{O})_n$ )
- negative nitrate ion hydrates ( $\text{NO}_3^-(\text{H}_2\text{O})_n$ )

At 10 km the average ion densities and masses are as follows [17]:

$$\begin{array}{lll} \text{Positive ions:} & n_+ \approx 2.5 \cdot 10^9 / \text{m}^3 & m_+ \approx 64 \text{ u} \\ \text{Negative ions:} & n_- \approx 2.5 \cdot 10^9 / \text{m}^3 & m_- \approx 77 \text{ u} \end{array}$$

### Plasma parameters

This data allows to calculate the Debye length, through equation [2.1]:  $\lambda_D \approx 15 \text{ mm}$ . Since the ion temperature is so low, and the E-Glider potential will easily be much higher, the collected current will be equal to the negative ion saturation current (the positive ions will be completely reflected). The saturation current density in these conditions can be calculated as:

$$J_{sat}^- = \frac{1}{4} q_e n_- \sqrt{\frac{8k_B T_-}{\pi m_-}} \approx 2.5 \cdot 10^{-8} \text{ A/m}^2 \quad (2.13)$$

## 2.5.3 System sizing

The charge/mass ratio required is quite high, therefore a very high electrode capacitance will be needed in order not to have excessively high electrode potentials.

Let's therefore assume for now a spherical electrode geometry, so that the capacitance is maximised and the boosting factor due to the Debye sheath acting as a spherical capacitor is maximised.

### Electrical parameters

The capacitance of a spherical electrode of radius  $R$  immersed in a plasma can be approximated as such:

$$C(R) = 4\pi\epsilon_0 (R|| - (R + \lambda_D)) \approx 4\pi\epsilon_0 \frac{R^2}{\lambda_D} \quad (2.14)$$

Where  $||$  is the parallel operator and the approximation is valid if  $\lambda_D \ll R$  (which will definitely be the case here).

The electrode potential can thus be calculated as a function of  $R$  and mass  $M$ :

$$V(R, M) = \frac{Q}{C} = M \left( \frac{Q}{M} \right) \frac{1}{C} \approx \frac{M}{R^2} \left( \frac{Q}{M} \right) \frac{\lambda_D}{4\pi\epsilon_0} \quad (2.15)$$

The total current can also be written as the integral of  $J_{sat}^-$  over the sheath surface:

$$I(R) = 4\pi(R + \lambda_D)^2 J_{sat}^- \approx 4\pi R^2 J_{sat}^- \quad (2.16)$$

Now the minimum total power needed to counteract the current collection can be expressed as the product of collected current and electrode potential:

$$P(R, M) = I(R) \cdot V(R, M) \approx M \left( \frac{Q}{M} \right) \frac{\lambda_D}{\epsilon_0} J_{sat}^- \approx M \cdot \underline{0.33 \text{ W/kg}} \quad (2.17)$$

This result indicates that, as long as all the assumptions made hold true, the power to mass ratio of the E-Glider blimp is independent of its physical dimensions, and can be achieved with available technology such as solar electric power generation.

### Breakdown voltage constraint

Since the required power is low and independent of the dimensions, the main concern for electrode sizing will probably be the limitation imposed by the atmospheric breakdown threshold.

This is the threshold electric field intensity over which the low-power Townsend discharge driven by the ion saturation current can cause an ionization avalanche in the neutral atmosphere molecules, and trigger a much more intense glow or arc discharge. The electric field in the Debye sheath can be very intense, and should the breakdown threshold be crossed, these high-current discharge could greatly increase the required power to maintain equilibrium, or even cause serious damage to the electrode.

Paschen's law allows to calculate the breakdown voltage for a given gap length and gas pressure. In this case the gap length is determined by the Debye length, and the pressure is the local atmospheric pressure reported in the previous section.

For a  $\text{CO}_2$  atmosphere such as that of Mars, the breakdown voltage across the Debye sheath at 10 km is [23]:

$$pd = p\lambda_D \approx 3.17 \text{ torr cm} \quad \implies \quad V_{BR} \approx 1 \text{ kV} \quad (2.18)$$

Other sources [7], however, report breakdown fields of 20 kV/m, that is  $\approx 0.3$  kV across the Debye gap. It must be noted, though, that the breakdown voltage depends on the gap length, and this figure was not associated with a relative gap length, therefore the experimental result [23] will be used as the reference.

In order not to exceed the breakdown voltage the following must hold:

$$V(R, M) < V_{BR} \implies \frac{M}{R^2} \frac{\lambda_D}{4\pi\epsilon_0} < V_{BR} \implies \frac{M}{R^2} < 7.5 \cdot 10^{-6} \text{ kg/m}^2$$

This equates to an electrode surface density  $\sigma < 0.6 \text{ mg/m}^2$ . This is not likely to be achieved with a full thin film surface (0.2 mils aluminized Mylar weights  $7000 \text{ mg/m}^2$ ), but could be achievable with a wire mesh.

If the wire spacing in this configuration weren't much greater than a Debye length, the capacitance wouldn't also be much decreased, thus avoiding even higher potentials that would require even thinner meshes.

A mesh of  $100 \mu\text{m}$  (human-hair width) strands of 0.5 mils thick aluminized Mylar, spaced 3 cm apart, if at all technically feasible, would achieve the required surface density limit.

## 2.5.4 Conclusions

Supposing a total mass of 1 kg, the E-Glider would have to deploy this extremely lightweight mesh in a spiderweb-like spheroidal surface with an equivalent radius of more than 300 m (a size comparable to the largest airships of the last century).

The technical challenges that such a design would impose are certainly daunting, even though not necessarily unachievable in the future. However careful research evaluation of options aimed at mitigating the breakdown constraint might drastically increase the feasibility of this concept.

One such option is to choose a **different levitation altitude**. Let's assume that reasonably strong atmospheric electric fields could be found at higher altitudes (this hypothesis should be verified, however the ionosphere should extend for several tens of kilometers), where the pressure is much lower.

With decreasing pressure, the breakdown voltage at first decreases until reaching a minimum, then very rapidly increases: high current discharges at very low pressures become practically impossible.

In these high altitude regions (e.g. 30 km to 50 km) the Debye length would be larger, and consequently the required potential would be higher as well. The breakdown voltage would however be far higher still, and the surface density constraint could be significantly relaxed.

Another option to explore is to **allow the glow discharge** to happen. Since required power is so low, it may well be possible that glow discharge could actually be manageable in terms of power (assuming the electrode was not damaged by the discharge) and

the breakdown threshold could be ignored.

However the variation in electrode capacitance would also have to be carefully evaluated, since a drop in capacitance would imply higher electrode voltages and perhaps a discharge runaway phenomenon.

It must also be noted that, while a martian application may prove unfeasible, it may very well be that with different conditions in **other atmospheres** the potential problem might be overcome.

Afterall, it is extremely encouraging that the required power is so low even though Mars already presents a significant gravity (surely far greater than an airless body). The advantage of exploiting atmospheric fields is that they can be very strong, while the gas ionization can be low enough that the collected current is not unbearably high.

The main limitation is once again due to high electrode potentials, but could be overcome if the atmosphere presented a high enough breakdown voltage. While data on the atmospheric electric properties of gas giants, Titan or Venus is scarce or absent, it could be that one of these may support E-Glider operations.

# Chapter 3

## Active Charge Control

### 3.1 Active electrostatic orbit control

One of the key features of the E-Glider concept is the ability to perform both orbit/-trajectory control and attitude control with the same (and virtually propellant-less) method of charge control.

Net and differential surface charging enables the E-Glider to generate forces and torques not only to maintain static equilibrium, but also to contrast disturbances and actively modify its trajectory or attitude to navigate around an airless body.

While past works have already modeled the effects of both net and differential charging, these analyses were focused on passive stability. A first demonstration model of the active control capabilities was therefore realized, in order to confirm and illustrate the concept validity.

#### 3.1.1 Reduction to 2D problem

Since most electrostatic fields and plasma data available to date is referred to a spherical asteroid model, an axial symmetry about the Sun-asteroid axis can be assumed for the electrostatic environment. If the gravity field is also axial-symmetric, the dynamics can be in first approximation reduced to a 2D space, with axes  $X$  (axial) and  $R$  (radial), and origin in the asteroid center.

Rigorously, this should be treated as a section of a cylindrical coordinate system. However, since all available data and dynamics models were obtained assuming a cartesian frame, and are not easily transported in a cylindrical frame, a further assumption that the reference frame can locally be treated as though it was cartesian is made.

Should the spacecraft dimensions be small if compared to the asteroid size, this could be a good approximation (especially in the terminator orbiting scenario). In any case it must also be noted that this is merely a validation of the envisioned approach to active control, not of the actual algorithms or simulation results, therefore some degree



of coarse approximation can be tolerated.

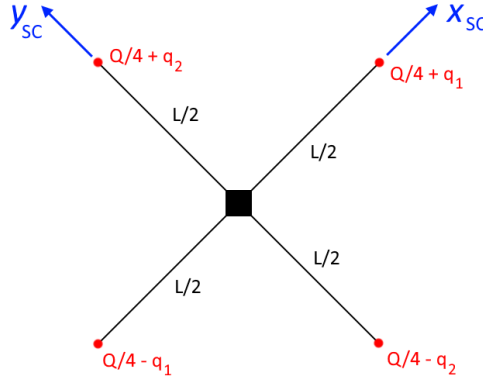


Figure 3.1: Simplified spacecraft model for the active control analysis

A simplified 2D spacecraft model is used (Figure 3.1), with four symmetrical electrodes around a central bus. The charge is only localized at the tip of the four appendages, each with length  $L/2$ , and its distribution is described by three variables:

- $Q$ , the "common mode" net spacecraft charge, equally distributed on the four electrodes.
- $q_1$ , the first "differential mode" charge, on the  $x$  axis electrode pair:  $+q_1$  on the electrode with positive  $x$  coordinate and  $-q_1$  on the electrode with negative  $x$  coordinate.
- $q_2$ , the second "differential mode" charge, on the  $y$  axis electrode pair:  $+q_2$  on the electrode with positive  $y$  coordinate and  $-q_2$  on the electrode with negative  $y$  coordinate.

### 3.1.2 Dynamics and control model

The position of the spacecraft is  $\mathbf{s}$ , while  $\theta$  represents the angle between the spacecraft  $x$  axis and the global  $X$  axis. These  $(\mathbf{s}, \theta)$  are the state variables.

The controller receives a certain commanded reference state  $(\mathbf{s}_0, \theta_0)$  and acts based on the error between this and the current state.

A PID controller is employed and translates the error in desired accelerations along the three state axes  $(\ddot{s}_X, \ddot{s}_R, \ddot{\theta})$ .

These acceleration commands are then translated with a custom fitting model into the actual control charges variables, i.e.  $(Q, q_1, q_2)$ .

Finally the system responds to the control variables following the dynamics equations. Figure 3.3 illustrates the control system in block diagram form.

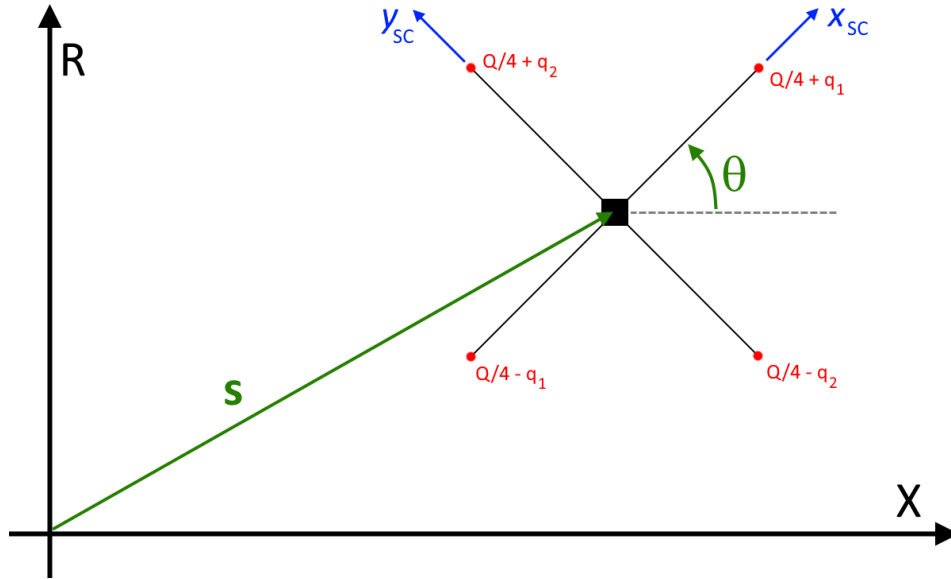


Figure 3.2: Reference frame and control variables for the active control analysis

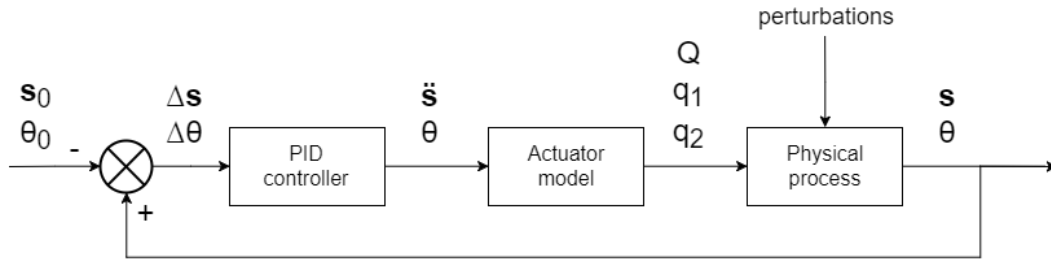


Figure 3.3: Block diagram of the active control system

### Physical process

The equations of motion can be adapted from those of [??] or [??] and [??], presented in the following chapter about full dynamics modeling. For simplicity's sake, the  $XR$  system is assumed to be inertial, and all terms due to the heliocentric orbital motion are discarded.

An angular momentum  $\mathbf{L}_X$  along  $X$  is assumed in order to simulate the centrifugal force  $\mathbf{f}_c$  due to electrostatic orbiting. This angular momentum is calculated for the equilibrium condition and kept constant, since no forces perpendicular to the  $XR$  plane are assumed to act on the spacecraft.

$$\begin{cases} m\ddot{\mathbf{s}} = \mathbf{f}_g + \mathbf{f}_p + \mathbf{f}_e + \mathbf{f}_c & (3.1a) \\ I_{mz}\ddot{\theta} = \mathbf{T}_g + \mathbf{T}_p + \mathbf{T}_e & (3.1b) \end{cases}$$

For the gravitational force a point-mass model is used. Torque around the  $\theta$  axis is null, because the inertia components  $I_{mx}$  and  $I_{my}$  are equal due to symmetry, and assuming

that  $x, y$  are principal axes the moment about that axis is only due to  $(I_{my} - I_{mx})$  (see equation [4.44]).

For the SRP, a simple cannonball model is assumed and basically a constant acceleration  $\mathbf{a}_p$  directed along  $X$  is imposed on the spacecraft.

As for the electrical effects, equations [4.58] and [4.61] apply. Torque around the  $\theta$  axis is null, because the inertia components  $I_{qx}$  and  $I_{qy}$  are equal<sup>1</sup>, and  $I_{qzx} = I_{qyz} = I_{qxy} = 0$  (see equation [4.62]).

The [3.1] can now be rewritten in more detail as follows:

$$\begin{cases} \ddot{\mathbf{s}} = -\frac{\mu}{s^3}\mathbf{s} + a_p\hat{\mathbf{X}} + \frac{Q}{m}\mathbf{E}(\mathbf{s}) + \mathbf{G}_e(\mathbf{s})\frac{\mathbf{S}_q}{m} + \frac{L_X}{r^3}\hat{\mathbf{R}} \\ \ddot{\theta} = (\mathbf{S}_q \times \mathbf{E}(\mathbf{s})) \cdot (\hat{\mathbf{X}} \times \hat{\mathbf{R}}) / I_{mz} \end{cases} \quad (3.2a)$$

$$\quad (3.2b)$$

NB: In this analysis,  $\mathbf{E}$  and  $\mathbf{G}_e$  are assumed to be bidimensional, i.e. only referred to  $X$  and  $R$  axes.

### Charge control actuation

In order to account for the charge which must be maintained at the static equilibrium condition and decouple that from the control variables,  $Q$  is split into two components:

$$Q = Q_0 + dq \quad | \quad \ddot{\mathbf{s}}(\mathbf{s}, Q, q_1, q_2) = \ddot{\mathbf{s}}(\mathbf{s}_0, Q_0, 0, 0) = 0 \quad (3.3)$$

That is,  $Q_0$  is the net charge that must be maintained at equilibrium, and  $dQ$  is the control component.

Now, assuming that  $\mathbf{s} \approx \mathbf{s}_0$ , [3.2] can be rewritten to directly link the control variables to the state accelerations:

$$\begin{cases} \ddot{\mathbf{s}} = \frac{dQ}{m}\mathbf{E}(\mathbf{s}) + \mathbf{G}_e(\mathbf{s})\frac{\mathbf{S}_q}{m} \\ \ddot{\theta} = (S_{qR}E_X(\mathbf{s}) - S_{qX}E_R(\mathbf{s})) / I_{mz} \end{cases} \quad (3.4a)$$

$$\quad (3.4b)$$

Or, more efficiently, in matrix form:

$$\begin{bmatrix} \ddot{\mathbf{s}} \\ \ddot{\theta} \end{bmatrix} = \begin{bmatrix} \mathbf{E}(\mathbf{s})/m & \mathbf{G}_e(\mathbf{s})/m \\ 0 & \mathbf{I}_\times \mathbf{E}(\mathbf{s})/I_{mz} \end{bmatrix} \begin{bmatrix} dQ \\ \mathbf{S}_q \end{bmatrix} \quad (3.5)$$

In which  $\mathbf{I}_\times$  is the unity skew-symmetric matrix.

The command vector  $(Q, q_1, q_2)$  can thus easily be derived from  $(dQ, \mathbf{S}_q)$ :

$$\begin{bmatrix} dQ \\ S_{qX} \\ S_{qR} \end{bmatrix} = \begin{bmatrix} 1 & 0 & 0 \\ 0 & L \cos \theta & -L \sin \theta \\ 0 & L \sin \theta & L \cos \theta \end{bmatrix} \begin{bmatrix} dQ \\ q_1 \\ q_2 \end{bmatrix} \quad (3.6)$$

---

1

This can be easily demonstrated by calculating the moments:

$$I_{qx} = [(Q/4 + q_2) + (Q/4 - q_2)]L^2/4 = QL^2/8$$

$$I_{qy} = [(Q/4 + q_1) + (Q/4 - q_1)]L^2/4 = QL^2/8$$

Therefore the [3.5] can be rewritten as:

$$\begin{bmatrix} dQ \\ q_1 \\ q_2 \end{bmatrix} = \begin{bmatrix} \mathbf{E}(\mathbf{s})/m & \mathbf{G}_e(\mathbf{s})/m \\ 0 & \mathbf{I}_\times \mathbf{E}(\mathbf{s})/I_{mz} \end{bmatrix}^{-1} \begin{bmatrix} 1 & 0 & 0 \\ 0 & \cos \theta/L & \sin \theta/L \\ 0 & -\sin \theta/L & \cos \theta/L \end{bmatrix} \begin{bmatrix} \ddot{s} \\ \ddot{\theta} \end{bmatrix} \quad (3.7)$$

Along the  $X$  axis, however, the first matrix is singular and therefore non-invertible. This is because along that axis, due to symmetry,  $E_R = G_{eXR} = G_{eRX} = G_{eRR} = 0$ , i.e.  $\ddot{s}_R = 0$  and can't be controlled.

To counter this issue, a deadband is set for values of  $|R| < R_{DB}$  and in these cases a simplified control law is used:

$$\begin{aligned} \begin{bmatrix} dQ \\ S_{qX} \\ S_{qR} \end{bmatrix} &= \begin{bmatrix} m\ddot{s}_R/E_X \\ 0 \\ I_{mz}\ddot{\theta}/E_X \end{bmatrix} \\ \begin{bmatrix} dQ \\ q_1 \\ q_2 \end{bmatrix} &= \begin{bmatrix} 1 & 0 & 0 \\ 0 & \cos \theta/L & \sin \theta/L \\ 0 & -\sin \theta/L & \cos \theta/L \end{bmatrix} \begin{bmatrix} m\ddot{s}_R/E_X \\ 0 \\ I_{mz}\ddot{\theta}/E_X \end{bmatrix} \end{aligned} \quad (3.8)$$

Since charges can't be chosen as arbitrarily large, saturation limits are imposed both on  $Q$  and  $q_1, q_2$ . If one of the latter saturates, however, the other is scaled as well in order to preserve the direction of  $\mathbf{S}_q$ , so as not to produce accelerations whose direction is too far off from the commanded one: an error in direction can be more detrimental than a simple decrease in magnitude.

It must be noted that throughout this process the local values of the electric field and gradient must be known in order to calculate the control vector. This, in a real E-Glider application, would be accomplished by means of auxiliary sensor electrodes acting as Langmuir probes.

### 3.1.3 PID Controller

The actual controller core, which commands the required accelerations given the state vector error is composed of three parallel PIDs which act independently on each axis. A PID is a simple controller whose output is formed by three components, respectively proportional to the input error itself (P), its integral in time (I) and its derivative (D).

The tuning of the PID coefficients can be tricky, and for this activity a combination of the Ziegler-Nichols method and trial and error was employed in order to achieve a satisfactory performance, however there's certainly room for improvement with more careful and precise tuning.

The integral component was only applied on the  $X$  axis, the other controllers turned out to be more properly PDs.

An anti-windup saturation limit was imposed on the integral component.

### Controller performance

Even with the raw controller tuning, the results indicate that it is indeed possible to control both position and attitude by means of active charge control.

The plots in the following pages display the response of the system to a starting condition severely offset from equilibrium.

The system converges to equilibrium with few to no oscillations along every axis.

The net charge required for the control, apart from some initial saturation spikes, is never too far from the equilibrium values, therefore the increase in power consumption for this kind of active operation can be considered negligible or anyway manageable, especially if the errors are kept small and the controller far from saturation (such as in a stationkeeping or slow sweeping situation).

### 3.1.4 Future work

Future work in this area would concern the expansion of the current model to a full 6-DOF control (three translations, three rotations), and perhaps test the expanded control algorithms in `AMOSPy`, which is well equipped to support this kind of controller.

It must be noted that in order to control the full 6-DOF state, another electrode pair perpendicular to the first two would not be sufficient, since it would only introduce 1 new control in spite of 3 new axes to be controlled.

Some other kind of pluri-electrode geometry, possibly with at least 5 or 6 electrode pairs should be implemented, in order to leverage not only the net charge  $Q$  and first moment of charge  $\mathbf{S}_q$ , but also the second moment of charge  $\mathbf{I}_q$ .

The control law for such a system would probably be quite complex, and it could be also worth investigating whether control over one or more axes could be safely relinquished, for a simplified configuration, or maybe substituted by other, passive stabilization means (e.g. gravity gradient based).

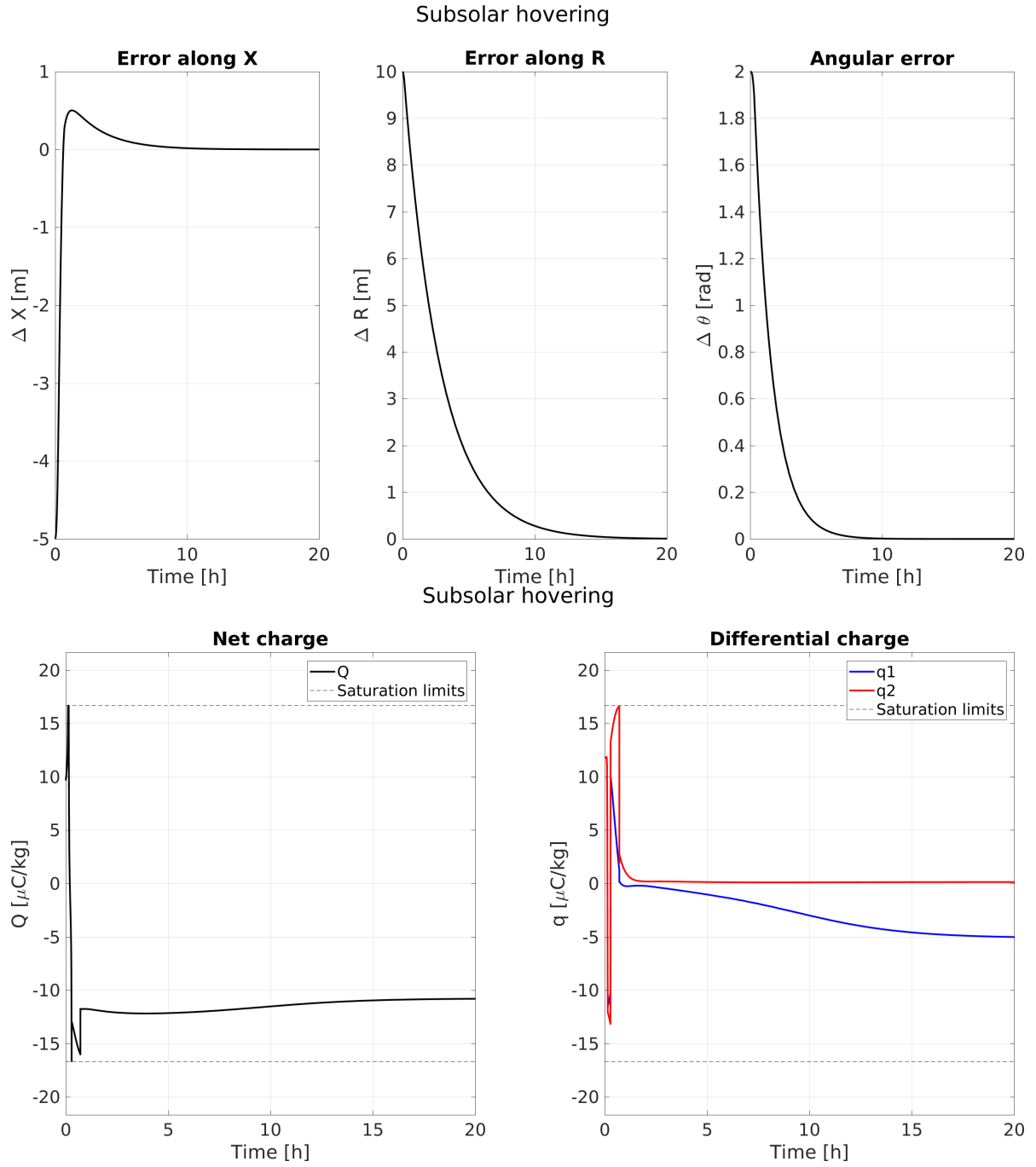


Figure 3.4: Time-history of active control errors and controls in a subsolar hovering scenario

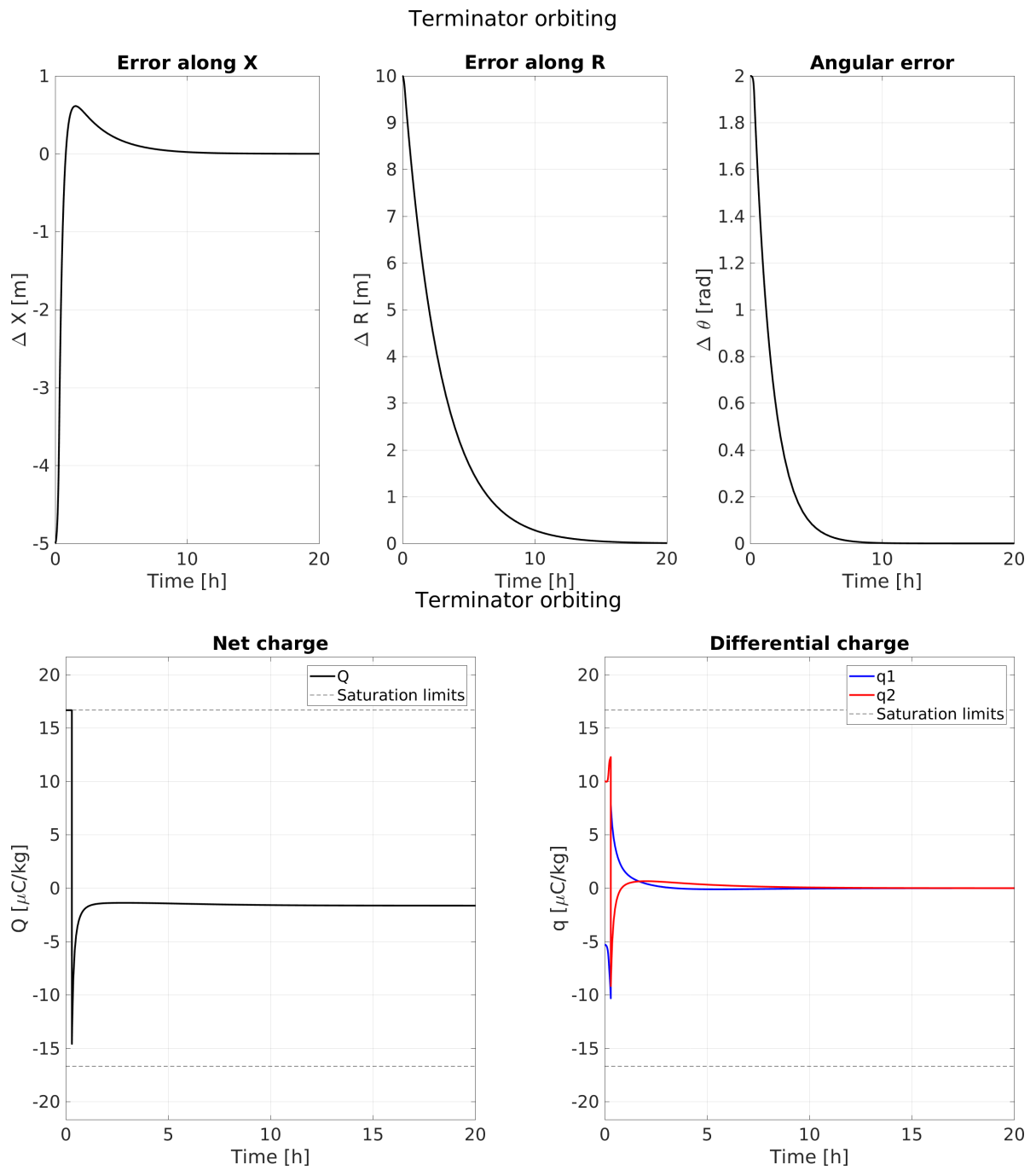


Figure 3.5: Time-history of active control errors and controls in a terminator orbiting scenario

# Chapter 4

## Dynamics Modeling and Simulation

### 4.1 Overview

A spacecraft dynamics simulator was developed with the objective of performing accurate trajectory and attitude simulations of an arbitrarily defined simple spacecraft (such as E-Glider concepts) in the proximity of an arbitrarily defined main body. It is named **AMOSPy**, for *Airless-body Multifield Orbital Simulator in Python*.

The "Multifield" attribute is to signify that not only gravitational, but also electrical and solar radiation pressure interactions are modeled, for both trajectory and attitude propagation (that is, forces and torques are calculated for each interaction).

AMOSPy is completely realized in **Python 2.7**. No modules except for those already included in the Fedora **Anaconda** distribution and the simulator own ones are needed.

AMOSPy is mostly programmed in an object-oriented style. Spacecrafts and main bodies are objects whose methods allow to simulate their interactions.

This makes the code more easily readable, easier to maintain and improve, and also allows to easily extend a single-spacecraft analysis to a multi-spacecraft one without having to radically change the code structure.

Some key features that were kept in high priority in the software development are flexibility, portability and maintainability. For instance, it is not mandatory to define electrical characteristics of the spacecraft if these are not needed. In this case **AMOSPy** will simulate a more "traditional" mission, only using gravitational and SRP interactions. As another example, the spacecraft is defined starting from elementary parts, so that arbitrarily shaped spacecrafts can be simulated.

Two simple auxiliary scripts are provided for Spacecraft and Main Body definition. Through a simple text UI the user can define step-by-step a new Spacecraft or Main Body instance, which is then saved to file. This allows to decouple the simulation objects definition from the simulation itself, and makes testing various spacecraft configurations very easy.



### 4.1.1 Code structure description

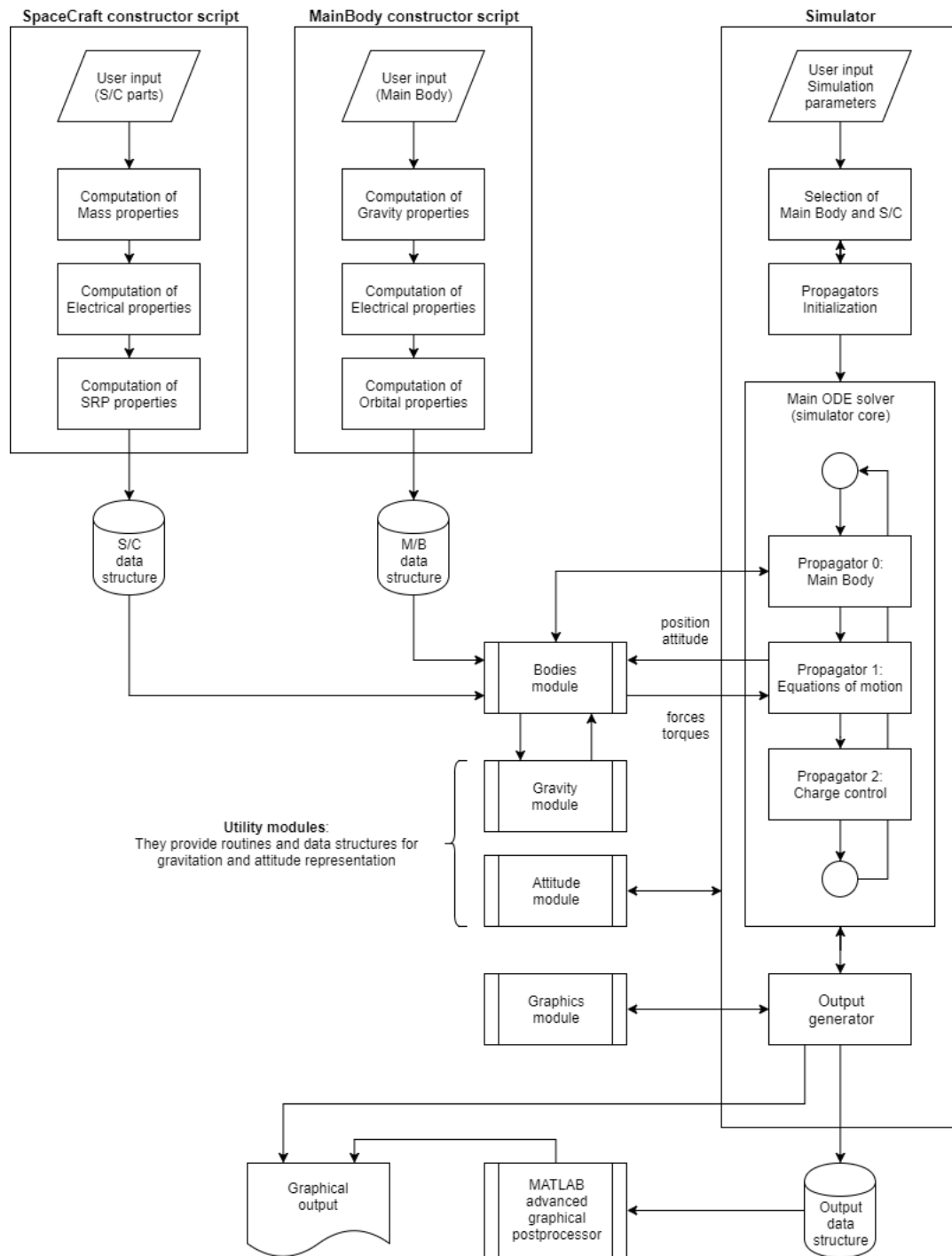


Figure 4.1: AMOSPy high-level structure.

### Spacecraft constructor

The Spacecraft constructor script allows to define a spacecraft through the addition of "parts", in a similar fashion to many multibody codes. Each part is based on a simple reference geometry, such as sphere, cuboid, plate or cylinder.

For each part, geometry, mass, electrical and SRP properties can be defined in detail. None of the properties is compulsory, in order to allow for high decoupling and flexibility. If one wishes to model a spherical part with a cuboidal electrode model, for instance, it can be done, simply by using a duplicate part with a cuboid geometry and only the desired electrical properties (while mass and SRP properties are only included in the original part).

### Main Body constructor

The Main Body constructor script allows to input main body parameters such as mass, geometry, gravity model (e.g. spherical harmonics), rotational and orbital parameters, and local plasma field data.

The orbital parameters can be directly obtained from the [JPL Small Bodies Database](#) [26].

The plasma data can be directly read from PIC simulations output, by means of specially formatted text files.

### Main Simulator core

The main simulator script simply contains some initialization sections (such as Spacecraft and Main Body loading routines), the main equation of motion and control model functions, and the ODE solver used to perform the simulation.

All other functions and routines are contained in the auxiliary modules described in the following paragraph, so as to declutter the main script and only leave the top-level functions.

Once provided with the simulation parameters (Spacecraft, Main Body, initial conditions and simulation time), the simulator propagates the equations of motion and the control functions.

The simulation results are both plotted and saved to disk in a MATLAB-compatible format. This data dump can later be used to produce high quality graphical outputs with the help of a MATLAB postprocessor.

As far as execution time is concerned, the simulator can easily perform in the real-time domain (i.e. the simulation is much faster than the simulated phenomenon).

By precalculating all spacecraft parameters (such as mass and charge inertia) and some external forces (SRP mesh, electric field mesh), good performance can be achieved. Particular attention was dedicated to implementing the fastest and most efficient algorithms

for those calculations which do not rely on precalculated data (such as gravitational interaction and keplerian propagation).

### Auxiliary Modules

Four main Python modules contain all the main classes and methods needed for the execution of AMOSPy, aside from the main simulation core.

The **bodies** module mainly contains the **SpaceCraft** and **MainBody** classes definitions. These define the object instances whose attributes are all the properties of the spacecraft or main body needed for the simulation.

Both classes contain propagator methods which are called by the main integrators and refresh various parameters.

For the **MainBody**, a fast keplerian orbit integrator is provided for the revolution motion [18]. The rotation motion, about any desired axis, is also implemented.

The **SpaceCraft** class also contains all the methods needed to compute the local gravitational, electrical and SRP forces and torques acting on the spacecraft itself.

A **Part** class used by the constructor scripts is also available in this module.

The **gravity** module is an appendix of the bodies module, and contains the keplerian orbit fast integrator as well as all the necessary gravity models calculators (for now, a point mass model and a fast nonsingular spherical harmonics model [?]) are available).

The **attitude** module provides ad-hoc quaternion and rotation matrix classes for attitude representation and propagation.

The **graphics** module provides some graphical routines for output generation.

## 4.2 Reference Frames

A first topic that must be addressed concerns the various reference frames used, in order to understand the dynamics models and to correctly write the equations of motion.

In order to express different vectorial quantities in the various available frames, the following notation is used:

- ${}^a\mathbf{x}$  indicates the vector or tensor  $\mathbf{x}$  expressed in the  $a$  frame.
- ${}^a\omega_{bc}$  indicates the angular velocity of frame  $c$  wrt frame  $b$  expressed in the  $a$  frame.
- ${}^a\mathbf{R}_b$  indicates the rotation matrix (tensor) which converts  ${}^b\mathbf{x}$  into  ${}^a\mathbf{x}$ .

It is worth spending some further words on these rotation matrices and their generation, since it will be useful in defining the reference frames relative orientations.

### 4.2.1 Rotation Matrices

The rotation matrix  ${}^a\mathbf{R}_b$  is a tensor which can convert vectors among the frames  $a$  and  $b$ . It is defined as such:

$${}^a\mathbf{R}_b \quad | \quad {}^a\mathbf{x} = {}^a\mathbf{R}_b {}^b\mathbf{x} \quad (4.1)$$

To define a rotation matrix, it is often useful to combine elementary rotations about the frame axes. Generally speaking, in  $\mathbb{R}^3$  three such rotations are able to describe the relative orientation of any two frames.

Two classical conventions based on this principle are the Euler and Tait-Bryan angles [5], of which the former is widely used in spaceflight dynamics while the latter is usually adopted in atmospheric flight dynamics.

Let's suppose that reference frame  $a$  can be overlapped over frame  $b$  by means of a sequence of  $n$  rotations of entities  $\alpha_i$  about axes  $k_i$ .

It must be noted that  $k_i$  is intended to be an axis of the rotated frame reached at the step  $i - 1$ , and not of the original  $a$  frame. That is to say:

- $a$  is rotated into  $a_1$  by a rotation of  $\alpha_1$  about axis  $k_1$  of  $a$ ;
- $a_1$  is rotated into  $a_2$  by a rotation of  $\alpha_2$  about axis  $k_2$  of  $a_1$ ;
- ...
- $a_{n-1}$  is rotated into  $b$  by a rotation of  $\alpha_n$  about axis  $k_n$  of  $a_{n-1}$ .

Then the rotation can be written as:

$${}^a\mathbf{R}_b = [\alpha_n]_{k_n} \dots [\alpha_2]_{k_2} [\alpha_1]_{k_1} = \prod_{i=1}^n [\alpha_i]_{k_i} \quad (4.2)$$

Depending on the value of  $k_i$  there are three kinds of possible elementary rotation matrices (one for each rotation axis). These are:

$$[\alpha]_1 = \begin{bmatrix} 1 & 0 & 0 \\ 0 & +\cos \alpha & -\sin \alpha \\ 0 & +\sin \alpha & +\cos \alpha \end{bmatrix} \quad (4.3a)$$

$$[\alpha]_2 = \begin{bmatrix} +\cos \alpha & 0 & +\sin \alpha \\ 0 & 1 & 0 \\ -\sin \alpha & 0 & +\cos \alpha \end{bmatrix} \quad (4.3b)$$

$$[\alpha]_3 = \begin{bmatrix} +\cos \alpha & -\sin \alpha & 0 \\ +\sin \alpha & +\cos \alpha & 0 \\ 0 & 0 & 1 \end{bmatrix} \quad (4.3c)$$

$$(4.3d)$$

With this notation, the Euler (3,1,3) and Tait-Bryan (3,2,1) conventions can be expressed respectively as:

$${}^b\mathbf{R}_a = [\gamma]_3 [\beta]_1 [\alpha]_3 \quad (4.4a)$$

$${}^b\mathbf{R}_a = [\phi]_1 [\theta]_2 [\psi]_3 \quad (4.4b)$$

$(\alpha, \beta, \gamma)$  are the Euler angles (e.g. precession, nutation and spin).

$(\psi, \theta, \phi)$  are the Tait-Bryan angles (e.g. yaw, pitch and roll).

### 4.2.2 Heliocentric Frames

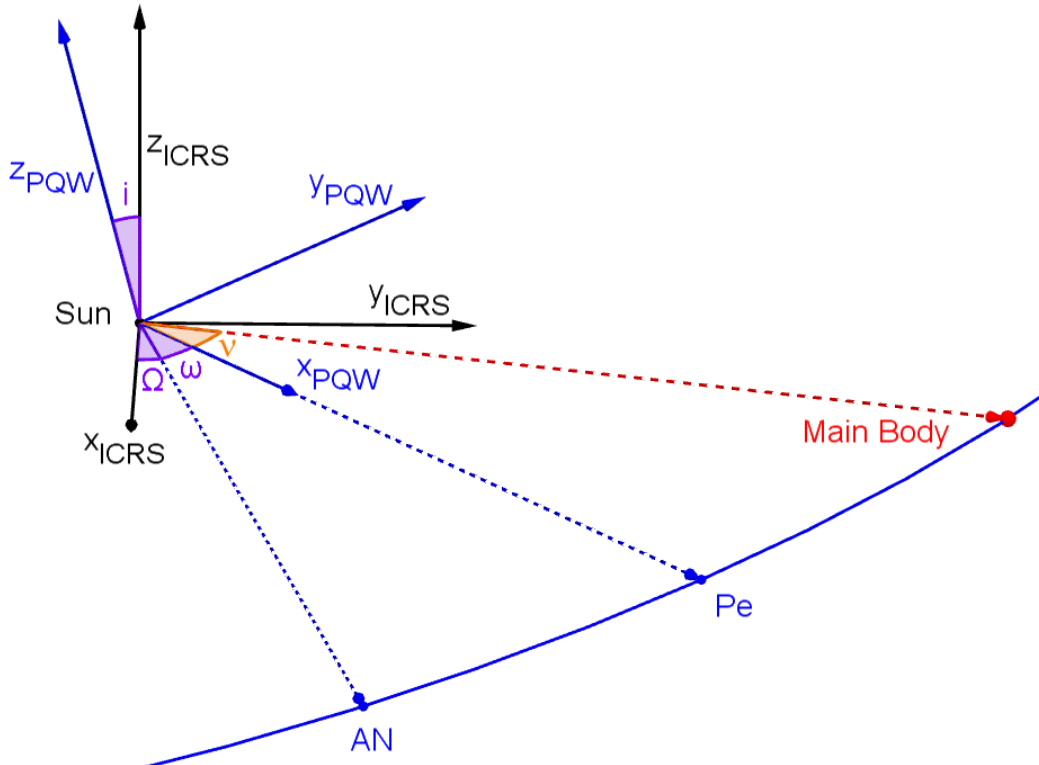


Figure 4.2: Heliocentric reference frames

#### ICRS Frame - $i$

The fundamental frame used in this work, from which all other frames are ultimately derived, is the International Celestial Reference System (ICRS). This is a quasi-inertial frame (inertial for the purposes of this work).

It is based on 212 extra-galactic radio sources, the position of which is known with an accuracy of 1 milliarcsecond or better. Since these sources are so far away, their intrinsic motion is assumed to be negligible, and this makes the ICRS "as inertial as possible".

The ICRS orientation approximates the equatorial system. A raw definition can thus be expressed as such:

- O origin at the Solar System Barycenter;
- X axis approximately pointing towards the vernal equinox at J2000;
- Y axis parallel to the Earth's Equator and completing the right handed frame;
- Z axis perpendicular to the Earth's Equator, pointing towards the North Pole.

### **PQW Frame - $p$**

Another heliocentric pseudo-inertial frame used is the Main Body perifocal reference frame. This is used to define the Main Body heliocentric orbit.

The Main Body orbit is assumed to be Keplerian in this work; the definition could however be extended to perturbed orbits, by assuming the osculating Keplerian orbit at the reference epoch.

It is defined as follows:

- O origin at the Solar System Barycenter;
- X axis pointing towards the periapsis;
- Y axis lying on the orbital plane and completing the dextral orthogonal system;
- Z axis parallel to the orbital angular momentum vector.

It can be derived from the ICRS frame by an Euler rotation based on the classical orbital elements of the Main Body:

$${}^p\mathbf{R}_i = [\omega]_3 [i]_1 [\Omega]_3 \quad (4.5)$$

In which:

- $\Omega$  is the right ascension of the ascending node (RAAN);
- $i$  is the orbital inclination;
- $\omega$  is the argument of periapsis.

### 4.2.3 Main Body Centered Frames

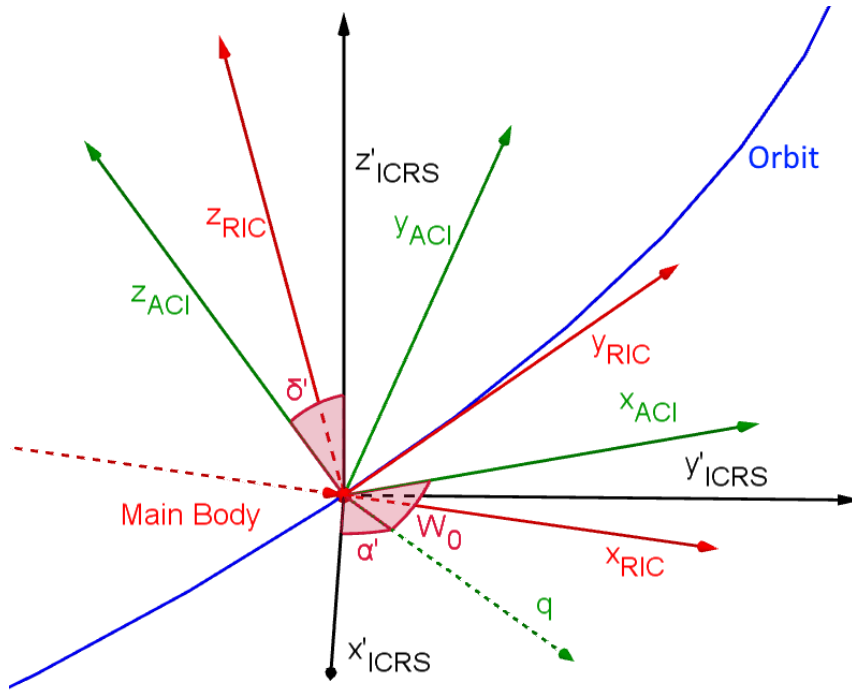


Figure 4.3: Main Body centered reference frames

#### RIC Frame - $r$

The Radial/In-track/Cross-track is a non-inertial frame, and it is the one used to write the translation equations of motion.

It is defined as follows:

- O origin at the Main Body center of mass;
- X axis directed away from the Solar System Barycenter (i.e. approximately away from the Sun);
- Y axis lying on the orbital plane and completing the dextral orthogonal system;
- Z axis parallel to the orbital angular momentum vector.

It can be derived from the PQW frame (translated to the Main Body) by simple time-dependent rotation due to the orbital motion:

$${}^r\mathbf{R}_p = [\nu(t)]_3 \quad (4.6)$$

In which  $\nu(t)$  is the true anomaly (i.e. orbital angular position) at time  $t$ .

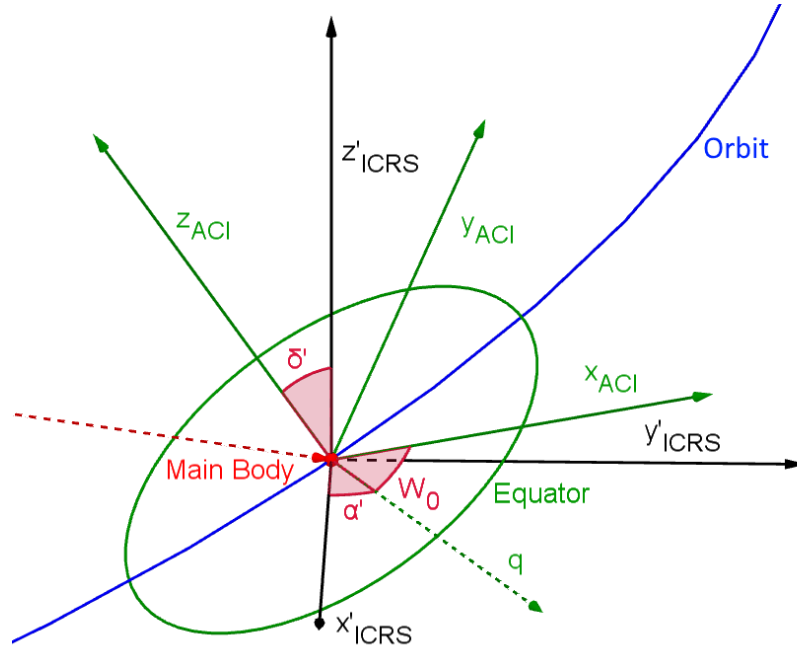


Figure 4.4: ACI reference frame definition

#### ACI Frame - *a*

The Aster-Centered Inertial is another pseudo-inertial frame, which is mainly used to define attitudes and rotations of the Spacecraft and the Main Body itself.

Indeed, the only non-inertial components are due to translation (since the origin is fixed on the Main Body), therefore no errors are introduced by considering it as inertial when referring attitudes to it.

It is defined as follows:

- O origin at the Main Body center of mass;
- X axis lying on the equator and pointing towards the prime meridian at the reference epoch;
- Y axis lying on the equator and completing the dextral orthogonal system;
- Z axis directed like the Main Body rotation angular momentum vector.

It can be derived from the ICRS frame (translated to the Main Body) by an Euler rotation based on the rotational elements [1]:

$$\begin{aligned} {}^a\mathbf{R}_i &= [W_0]_3 [\delta']_1 [\alpha']_3 \\ &= [W_0]_3 [90^\circ - \delta_0]_1 [90^\circ + \alpha_0]_3 \end{aligned} \quad (4.7)$$

In which:



- $\alpha_0$  is the right ascension of the positive pole;
- $\delta_0$  is the declination of the positive pole;
- $W_0$  indicates the position of the prime meridian at the reference epoch.

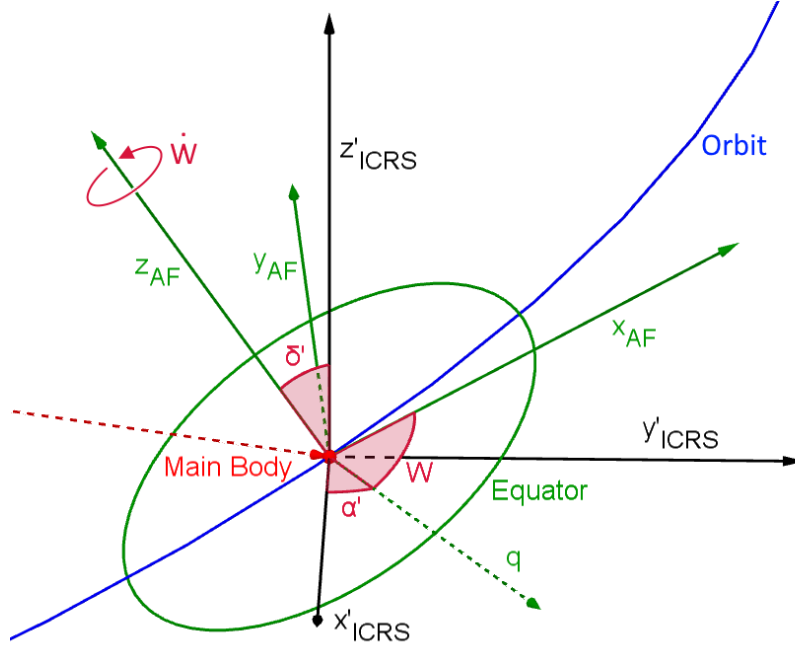


Figure 4.5: AF reference frame definition

### AF Frame - $f$

The Aster-Fixed is a reference frame fixed to the Main Body. The analogue for Earth would be the ECEF frame.

It is defined as follows:

- O origin at the Main Body center of mass;
- X axis lying on the equator and pointing towards the prime meridian;
- Y axis lying on the equator and completing the dextral orthogonal system;
- Z axis directed like the Main Body rotation angular momentum vector.

It can be derived from the ACI frame by a simple time-dependent rotation about the rotation axis:

$${}^f\mathbf{R}_a = [W(t) - W_0]_3 \quad (4.8)$$

In which  $W(t)$  is the position of the prime meridian at time  $t$ .

### 4.2.4 Spacecraft Centered Frames

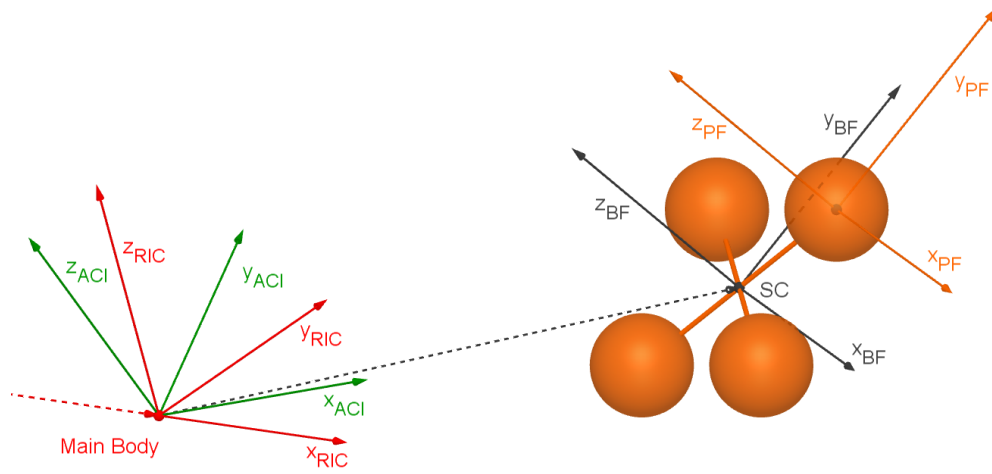


Figure 4.6: Spacecraft centered reference frames

#### BF Frame - $b$

The Body-Fixed is a reference frame fixed to the Spacecraft. It is used in defining parts placement during the Spacecraft definition, with one caveat: when a spacecraft design is finalized this frame is re-centered on the spacecraft center of mass, and the parts positions are recalculated as needed.

The Body Frame is used to propagate the attitude equations of motion: the attitude and rotation rates considered are intended to be between the BF and ACI frames, and are expressed in the BF frame.

It is defined as follows:

- O origin at the Spacecraft center of mass;
- Axes as defined by the user placement of parts.

Its orientation with respect to the ACI frame is defined with an attitude quaternion  ${}^b\mathbf{q}_a$ .

#### PF Frame - $p$

The Part-Fixed is a reference frame fixed to a single spacecraft elementary component, or part. It is used in defining parts dimensions, orientation and properties during the Spacecraft definition.

It is defined as follows:

- O origin at the Part center of mass;
- Axes parallel to the BF frame.

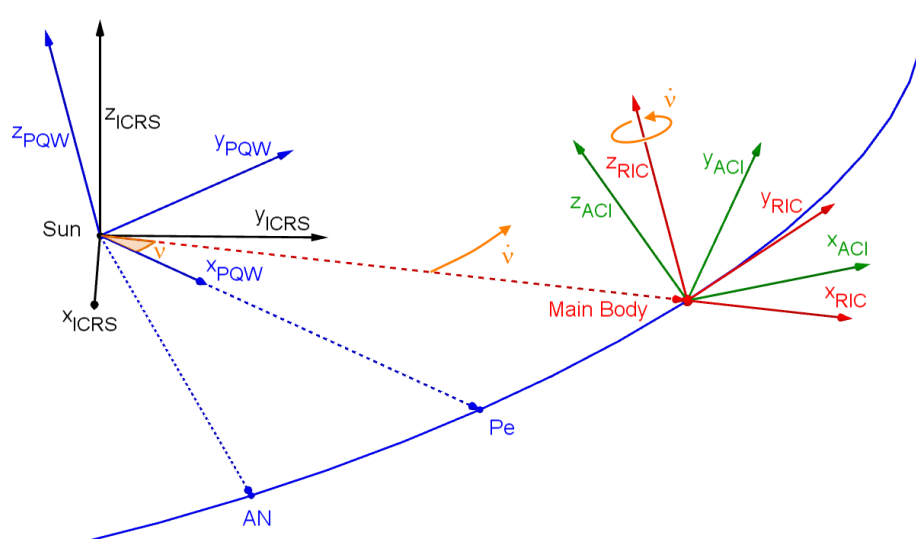


Figure 4.7: Overview of the definition of the main reference frames for the integration (ACI and RIC)

### 4.3 Integrator core

The core of **AMOSPy** is of course its numerical integrator of the equations of motion. Most other functions and modules are entirely built around it.

A real-valued variable-coefficient ODE solver is used, which provides automatic switching between implicit Adams method and a backwards differentiation formulation in case of problem stiffness.

**AMOSPy**'s integrator can operate in several configurations: considering the Spacecraft either a point or an extended body (basically switching on or off the attitude propagation), and using either the Clohessy-Wiltshire equations or a more exact "full model" for the three-body dynamics.

In this section only the extended body version of the equations of motion will be presented, since the point body can simply be obtained by removing the attitude propagation equation.

The state vector used for this full integration is:

$$({}^r\mathbf{r}, {}^r\mathbf{v}, {}^bq_a, {}^b\omega_{ab}) \quad (4.9)$$

That is, position, velocity, attitude quaternion and angular rates. The indices  $r$ ,  $b$ ,  $a$ , indicate respectively the Hill reference frame (Radial/In-track/Cross-track), the Aster-Centered Inertial frame (used as inertial frame for attitude reference) and the Spacecraft Body Frame, as described in section 4.2.

### 4.3.1 First cardinal equation

#### Clohessy-Wiltshire formulation

The Clohessy-Wiltshire equations describe the relative motion of two bodies, a target and a chaser, orbiting a third one. These equations are formulated in the Hill, or RIC, reference frame, fixed on the target.

Considering the typical case of this study of an E-Glider orbiting an asteroid on an heliocentric trajectory, the asteroid would be the target, the E-Glider the chaser and the Sun the third body.

The strong hypothesis assumed by the Clohessy-Wiltshire equations is that the target is in an unperturbed circular orbit around the third body, with angular velocity (mean motion)  $\dot{\nu} = n$ . In this case the RIC frame moves in a simple circular uniform motion, inducing centrifugal and Coriolis effects on the chaser spacecraft. The first cardinal equation of dynamics can be written like this:

$${}^r\dot{\mathbf{v}} = \frac{{}^r\mathbf{f}}{m} + 2n \begin{bmatrix} +v_i \\ -v_r \\ 0 \end{bmatrix} + n^2 \begin{bmatrix} +3r_r \\ 0 \\ -r_c \end{bmatrix} \quad (4.10)$$

$${}^r\dot{\mathbf{r}} = {}^r\mathbf{v} \quad (4.11)$$

In which  ${}^r\mathbf{r}$ ,  ${}^r\mathbf{v}$  are respectively the position and velocity of the chaser in the RIC frame, expressed in RIC coordinates. The single components are  ${}^r\mathbf{r} = (r_r, r_i, r_c)$  and  ${}^r\mathbf{v} = (v_r, v_i, v_c)$ .

${}^r\mathbf{f}$  represents the active forces on the spacecraft, again expressed in the RIC frame. In this case they could be the gravitational attraction of the Main Body, the solar radiation pressure force and the electrostatic force. Derivations for all these components can be found in the sections [4.4](#), [4.5](#), [4.6](#).

#### Full model formulation

This version of the equations of motion gets rid of the strong hypothesis imposed by the Clohessy-Wiltshire equations, allowing for arbitrary orbits around the third body.

The RIC frame motion is locally approximated to the second order (i.e. with a constant acceleration). In order to do this, the instantaneous orbital angular velocity and acceleration, as well as the distance from the third body, must be calculated.

For this reason, the orbit of the target (Main Body) must be propagated with a keplerian solver. A fast, third-order, orbit integrator [\[18\]](#) is therefore implemented in AMOSPy. This allows to calculate the true anomaly as a function of time  $\nu = \nu(t)$ .

Let  $d$  be the Sun to Main Body distance (or Sun to Spacecraft distance, they can safely approximated to be equal),  $\dot{\nu}$  and  $\ddot{\nu}$  respectively the *instantaneous* asteroid orbital angular velocity and acceleration.

Furthermore, let  $p$  be the semilatus rectum,  $h$  the angular momentum and  $e$  the eccentricity, of the Main Body keplerian orbit around the Sun. These are all constants that

can be precalculated during the Main Body definition.

Then for this keplerian orbit, knowing  $\nu = \nu(t)$  from the propagator, one can obtain:

$$d = \frac{p}{1 + e \cos \nu} \quad (4.12)$$

$$\dot{\nu} = \frac{h}{d^2} \quad (4.13)$$

$$\ddot{\nu} = \frac{-2e \sin \nu}{1 + e \cos \nu} \dot{\nu}^2 \quad (4.14)$$

In order to write the first equation of motion in the RIC frame the acceleration of the Spacecraft in that frame must be calculated, taking into account the apparent accelerations due to the frame motion, as previously noted.

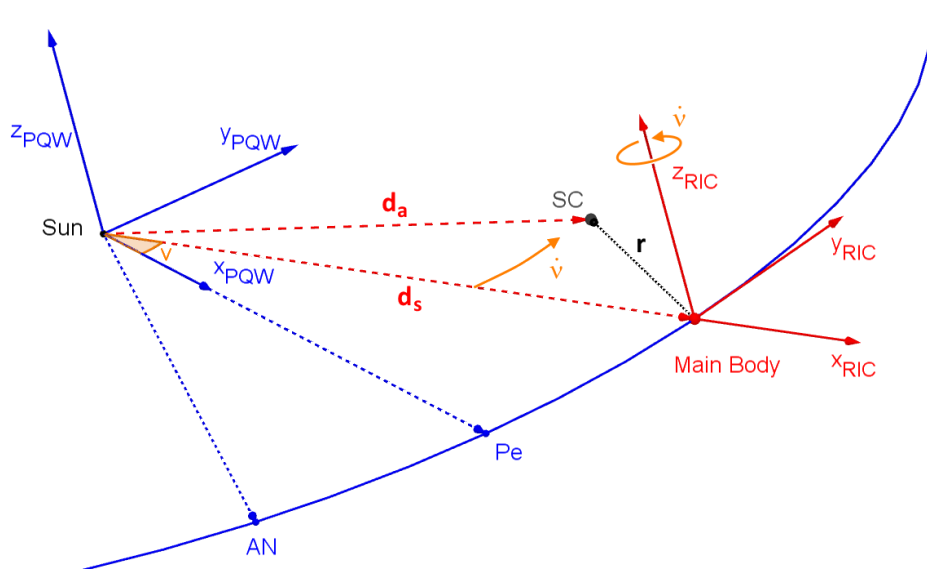


Figure 4.8: Vector definitions for the full model

Let  $\mathbf{r}$  be the position of the Spacecraft referred to the Main Body, while  $\mathbf{d}_s$  and  $\mathbf{d}_a$  are respectively the Sun to Spacecraft and the Sun to Main Body position vectors, as shown in Figure 4.8.

The PQW frame will serve as the inertial reference frame.  $\boldsymbol{\Omega}$  is the angular velocity of the RIC frame with respect to the PQW frame. From the relations among the reference frames detailed in section 4.2 it can be shown that:

$${}^r\boldsymbol{\Omega} = (0, 0, \dot{\nu}) \quad (4.15a)$$

$${}^r\dot{\boldsymbol{\Omega}} = (0, 0, \ddot{\nu}) \quad (4.15b)$$

Now the absolute acceleration of the spacecraft can be expressed as follows:

$$\begin{aligned}\mathbf{d}_s &= \mathbf{d}_a + \mathbf{r} \\ \ddot{\mathbf{d}}_s &= \ddot{\mathbf{d}}_a + \ddot{\mathbf{r}} \\ \ddot{\mathbf{d}}_s &= \ddot{\mathbf{d}}_a + \mathbf{a} + 2\boldsymbol{\Omega} \times \mathbf{v} + \boldsymbol{\Omega} \times (\boldsymbol{\Omega} \times \mathbf{r}) + \dot{\boldsymbol{\Omega}} \times \mathbf{r}\end{aligned}\tag{4.16}$$

In which  $\mathbf{r}$ ,  $\mathbf{v}$ ,  $\mathbf{a}$  are respectively the position, velocity and acceleration relative to the RIC frame, which appear in the equation of motion. The terms derived from  $\ddot{\mathbf{r}}$  are respectively the local acceleration, the Coriolis and centrifugal terms and lastly a term due to the angular acceleration of the frame (from the second order expansion of orbital motion).

Solving for  $\mathbf{a}$  the resulting equation is:

$$\mathbf{a} = \ddot{\mathbf{d}}_s - \ddot{\mathbf{d}}_a - 2\boldsymbol{\Omega} \times \mathbf{v} - \boldsymbol{\Omega} \times (\boldsymbol{\Omega} \times \mathbf{r}) - \dot{\boldsymbol{\Omega}} \times \mathbf{r}\tag{4.17}$$

It can now be noted that  $\ddot{\mathbf{d}}_a$  is the inertial acceleration of the Main Body, which is only due to the Sun's gravitational acceleration. Another term due to the Sun's gravitational acceleration can be extracted from  $\ddot{\mathbf{d}}_s$ , with the remainder being accelerations due to the Main Body gravity, local electric field, and SRP.

Letting  $\mu$  be the Sun's gravitational parameter, the [4.17] now becomes:

$$\mathbf{a} = \frac{\mathbf{f}}{m} - \frac{\mu}{d_s^3} \mathbf{d}_s + \frac{\mu}{d_a^3} \mathbf{d}_a - 2\boldsymbol{\Omega} \times \mathbf{v} - \boldsymbol{\Omega} \times (\boldsymbol{\Omega} \times \mathbf{r}) - \dot{\boldsymbol{\Omega}} \times \mathbf{r}\tag{4.18}$$

$$\mathbf{a} = \frac{\mathbf{f}}{m} - \frac{\mu}{d^3} \mathbf{r} - 2\boldsymbol{\Omega} \times \mathbf{v} - \boldsymbol{\Omega} \times (\boldsymbol{\Omega} \times \mathbf{r}) - \dot{\boldsymbol{\Omega}} \times \mathbf{r}\tag{4.19}$$

The [4.17] assumes that  $d_s \approx d_a$ , which is a valid assumption, since for proximity operations  $r \ll d_s, d_a$ .

As the final step, the equations [4.15] (and implicitly [4.12], [4.13], [4.14]) are substituted into the [4.19].

The first cardinal equation for the full model, in RIC components, then turns out to be:

$${}^r\dot{\mathbf{v}} = \frac{{}^r\mathbf{f}}{m} + \frac{\mu}{d^3} {}^r\mathbf{r} + 2\dot{\nu} \begin{bmatrix} -v_i \\ +v_r \\ 0 \end{bmatrix} + \dot{\nu}^2 \begin{bmatrix} +r_r \\ +r_i \\ 0 \end{bmatrix} + \ddot{\nu} \begin{bmatrix} -r_i \\ +r_r \\ 0 \end{bmatrix}\tag{4.20}$$

$${}^r\dot{\mathbf{r}} = {}^r\mathbf{v}\tag{4.21}$$

In which  ${}^r\mathbf{r}$ ,  ${}^r\mathbf{v}$  are respectively the position and velocity of the chaser in the RIC frame, expressed in RIC coordinates. The single components are  ${}^r\mathbf{r} = (r_r, r_i, r_c)$  and  ${}^r\mathbf{v} = (v_r, v_i, v_c)$ .

${}^r\mathbf{f}$  represents the active forces on the spacecraft, again expressed in the RIC frame. In this case they could be the gravitational attraction of the Main Body, the solar radiation pressure force and the electrostatic force. Derivations for all these components can be found in the sections 4.4, 4.5, 4.6.

### 4.3.2 Second cardinal equation

The attitude propagation equation is derived from classical rigid body theory. The only quirk of this formulation is that attitude is represented as a quaternion in order to avoid singularities (for further details see appendix A1).

$${}^b\dot{\omega}_{ab} = {}^b\mathbf{I}_m^{-1}({}^b\mathbf{T} - {}^b\omega_{ab} \times {}^b\mathbf{I}_m {}^b\omega_{ab}) \quad (4.22)$$

$${}^b\dot{\mathbf{q}}_a = \frac{1}{2} \begin{bmatrix} 0 \\ {}^b\omega_{ab} \end{bmatrix} \otimes {}^b\mathbf{q}_a \quad (4.23)$$

${}^b\omega_{ab}$  is the ACI to BF angular velocity in BF coordinates, while  ${}^b\mathbf{q}_a$  is the ACI to BF attitude quaternion.  ${}^b\mathbf{I}_m$  is the Spacecraft moment of inertia.  $\otimes$  is the quaternion product (see A1).

${}^b\mathbf{T}$  represents the active torques on the Spacecraft. In this case they could be due to the gravitational attraction of the Main Body, the solar radiation pressure and the electrostatic interactions. Derivations for all these components can be found in the sections 4.4, 4.5, 4.6.

It must lastly be noted that the attitude quaternion must be normalized at each integration step to avoid divergence. A check is performed anyway and should the quaternion norm grow through a certain threshold, an exception is raised by the software.

### 4.3.3 Control equations

A control function call is present in the integrator core, and a "plug-and-play" control function space is reserved for future implementation and testing of active charge control functions. This function has access to the current simulation time and state vector as well as all the properties of the Spacecraft and the Main Body, refreshed at the current simulation time.

## 4.4 Gravitational forces modeling

### 4.4.1 Point-Mass model

Perhaps the simplest way to model the gravitational field of a massive body is the point-mass model; this assumes that all the body mass is concentrated in its barycenter. The gravitational acceleration in this model is purely radial, and expressed by the following equation:

$$\mathbf{f}_g = -\frac{\mu}{r^3}\mathbf{r} \quad (4.24)$$

In which  $\mu \doteq GM$  is the gravitational parameter of the main body and  $\mathbf{r}$  is the position vector with origin in the main body barycenter.

The gravity gradient tensor can be calculated as follows [9]:

$$\mathbf{G}_g \doteq \nabla \mathbf{f}_g = -\frac{\mu}{r^3} \left( \mathbf{I} - \frac{3}{r^2} \mathbf{r} \otimes \mathbf{r} \right) \quad (4.25)$$

Where  $\otimes$  indicates the outer product.

#### Point-Mass pros and cons

The point-mass model is a mathematically exact equivalence for bodies with a spherically symmetrical mass distribution, and therefore acceptably accurate as a first approximation for large bodies such as planets, however it is generally largely inaccurate for asteroids, comets and other such small bodies, whose geometries and density distributions are often very irregular.

Its advantages in the field of dynamics modeling are however its extremely low computational cost and its intrinsic absence of singularities. Thus, while not a good choice for precise mission simulations (in which a specific main body and its properties are given), it can still be a valid option for general analyses and feasibility studies. In the case of this work, for instance, the reference asteroid for the PIC plasma data is in fact spherical, and a point-mass model can be applied without much concern.

#### 4.4.2 Spherical Harmonics model

Another widely used method to model a gravitational field is the expansion in spherical harmonics. In this case a gravitational potential function  $U_g$  |  $\nabla U_g = \mathbf{a}_g$ , where  $\mathbf{a}_g$  is the gravitational acceleration, can be written as:

$$U_g = \frac{\mu}{r} \sum_{n=0}^{\infty} \sum_{m=0}^n \left( \frac{R}{r} \right)^n P_{n,m}(\sin \phi) (C_{n,m} \cos \lambda + S_{n,m} \sin \lambda) \quad (4.26)$$

In which  $R$  is a reference radius, while  $C_{n,m}$  and  $S_{n,m}$  are the spherical harmonics coefficients which parametrize the expansion.  $\phi$ ,  $\lambda$  are respectively the latitude and longitude of the considered point  $\mathbf{r}$  in spherical coordinates.  $P_{n,m}$  are the Legendre polynomials, defined as follows:

$$P_{n,m}(\sin \phi) = (1 - \sin^2 \phi)^{m/2} \frac{1}{2^n n!} \frac{d^{n+m}}{d \sin \phi^{n+m}} (\sin^2 \phi - 1)^n \quad (4.27)$$

Assuming that the reference system is centered in the main body barycenter, the following relations are valid:

$$\begin{array}{llll} C_{00} = 1 & C_{10} = 0 & C_{11} = 0 & C_{n0} \doteq -J_n \\ S_{00} = 0 & S_{10} = 0 & S_{11} = 0 & \end{array}$$

Often  $C$  and  $S$  coefficients are given in a normalized form, in order to avoid too large a span in orders of magnitude: they tend to become very small with increasing order  $n$ .



These normalized forms,  $\overline{C}_{n,m}$  and  $\overline{S}_{n,m}$  are defined as follows [6]:

$$\overline{C}_{n,m} \doteq \frac{C_{n,m}}{N_{n,m}} \quad \overline{S}_{n,m} \doteq \frac{S_{n,m}}{N_{n,m}} \quad N_{n,m} \doteq \sqrt{\frac{(n-m)!}{(n+m)!} (2n+1)(2-\delta_{0,m})} \quad (4.28)$$

The formulation given in [4.26], however, presents an issue when used to calculate the gravitational acceleration, because  $\mathbf{a}_g = \nabla U_g$  and the  $\nabla$  operator in spherical coordinates presents a singularity at the poles ( $\phi = \pm\pi/2$ ). Since the terminator region is of particular interest for the E-Glider concept, and this includes the poles, such singularity cannot be neglected.

A nonsingular formulation of spherical harmonics is therefore required; several of these exist, with the main ones proposed by Pines (1973), Lear (1986) and Gottlieb (1990). The one presented here and implemented in AMOSPy is that of Pines [20], with a corrected Legendre polynomials recursion (the original one proposed by Pines is unstable [6][14]).

Pines' formulation uses a redundant set of 4 coordinates based on a cartesian reference frame and defined as follows:

$$(r, s, t, u) \quad | \quad \mathbf{r} = r \cdot \begin{bmatrix} s \\ t \\ u \end{bmatrix}, \quad \|\mathbf{r}\| = r \quad (4.29)$$

Equation [4.26] thus becomes:

$$U_g = \frac{\mu}{r} \sum_{n=0}^{\infty} \sum_{m=0}^n \left( \frac{R}{r} \right)^n A_{n,m}(u) (C_{n,m} r_m(s, t) + S_{n,m} i_m(s, t)) \quad (4.30)$$

The  $r_m$  and  $i_m$  terms replace the goniometric functions of the longitude and are defined as:

$$r_m(s, t) = \text{Re}((s + it)^m) \quad i_m(s, t) = \text{Im}((s + it)^m) \quad (4.31)$$

The terms  $A_{n,m}$  are instead derived from the Legendre polynomials and are called Legendre functions:

$$A_{n,m}(u) = \frac{1}{2^n n!} \frac{d^{n+m}}{du^{n+m}} (u^2 - 1)^n \quad (4.32)$$

An efficient and stable recursion algorithm used to calculate these functions is presented in [14] (variant II):

$$A_{n,n} = 2(n-1)A_{n-1,n-1} \quad (4.33a)$$

$$A_{n,n-1} = uA_{n,n} \quad (4.33b)$$

$$A_{n,m} = \frac{1}{(n-m)(n+m+1)} [2u(m+1)A_{n,m+1} + (u^2 - 1)A_{n,m+2}] \quad (4.33c)$$

The values of  $A_{m,n}$  can be stored in a  $N \times M$  matrix, in which  $N, M$  are the maximum orders of the model used. The first formula is then used to populate the main diagonal, the second one for the first subdiagonal and the last one for all the remaining values, by rows.

In order to calculate the gravitational force, the [4.30] must be differentiated as follows:

$$\begin{aligned} \mathbf{a}_g = \nabla U_g = & \left( \frac{1}{r} \frac{\partial U_g}{\partial s} \right) \hat{\mathbf{i}} + \left( \frac{1}{r} \frac{\partial U_g}{\partial t} \right) \hat{\mathbf{j}} + \left( \frac{1}{r} \frac{\partial U_g}{\partial u} \right) \hat{\mathbf{k}} + \\ & + \left( \frac{\partial U_g}{\partial r} - \frac{s}{r} \frac{\partial U_g}{\partial s} - \frac{t}{r} \frac{\partial U_g}{\partial t} - \frac{u}{r} \frac{\partial U_g}{\partial u} \right) \hat{\mathbf{r}} \end{aligned} \quad (4.34)$$

By redefining the versor coefficients respectively as  $a_1, a_2, a_3, a_4$  one can write:

$$\mathbf{a}_g = \nabla U_g = a_1 \hat{\mathbf{i}} + a_2 \hat{\mathbf{j}} + a_3 \hat{\mathbf{k}} + a_4 \hat{\mathbf{r}} \quad (4.35)$$

$$\mathbf{G}_g = \nabla \mathbf{a}_g = \frac{\partial}{\partial \mathbf{r}} (a_1 \hat{\mathbf{i}} + a_2 \hat{\mathbf{j}} + a_3 \hat{\mathbf{k}} + a_4 \hat{\mathbf{r}}) \quad (4.36)$$

Pines [20] presents in his paper computationally efficient methods for calculating these quantities in software, and these are implemented in AMOSPy, however they are not detailed here for coincisness reasons.

### Spherical Harmonics pros and cons

The spherical harmonics expansion guarantees convergence to any possible gravitational potential, however the convergence is usually quite slow and very high orders are required to accurately model complex fields and fine details. Moreover the expansion diverges at radii smaller than the reference radius, so it's usually not ideal to use spherical harmonics for bodies with large concave features (such as asteroids, incidentally). Nevertheless, spherical harmonics allow to capture tangential components of the gravitational field, and can provide an accuracy orders of magnitude greater than a point-mass model with a modest increase in computational power (if compared to more sophisticated methods such as FE MASCON).

#### 4.4.3 Forces and Torques

Whatever the gravitational model assumed, the simulator must be able to calculate forces and torques applied on the S/C given the local gravitational acceleration  $\mathbf{a}_g$  and gravity gradient  $\mathbf{G}_g$ .

### Force

Since the spacecraft is treated as an extended body, the force due to gravity is calculated as follows:

$$\mathbf{f}_g = \int_{S/C} \mathbf{a}_g(\mathbf{r}) \, dm \quad (4.37)$$

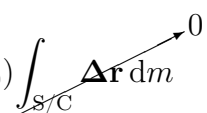
The spacecraft can either be considered as an extended body characterized by a mass and a moment of inertia, or as a collection of parts, the masses of which are approximated to be concentrated in their centers of mass.

In the former case a linear approximation of the local gravitational field is assumed:

$$\Delta \mathbf{r} \doteq \mathbf{r} - \mathbf{r}_0 \quad (4.38)$$

$$\mathbf{a}_g(\mathbf{r}) = \mathbf{a}_g(\mathbf{r}_0) + \mathbf{G}_g(\mathbf{r}_0) \Delta \mathbf{r} \quad (4.39)$$

In which  $\mathbf{r}_0$  is the position of the spacecraft center of mass. Equation [4.37] can then be expressed as follows:

$$\begin{aligned} \mathbf{f}_g &= \int_{S/C} [\mathbf{a}_g(\mathbf{r}_0) + \mathbf{G}_g(\mathbf{r}_0) \Delta \mathbf{r}] \, dm \\ &= \mathbf{a}_g(\mathbf{r}_0) \int_{S/C} dm + \mathbf{G}_g(\mathbf{r}_0) \int_{S/C} \Delta \mathbf{r} \, dm \\ &= \mathbf{a}_g(\mathbf{r}_0) m \end{aligned} \quad (4.40)$$


The diagram shows a vector  $\Delta \mathbf{r}$  originating from a point  $\mathbf{r}_0$  and pointing to a point  $\mathbf{r}$ . A coordinate system  $0$  is indicated by an arrow pointing towards the right.

The second integral can be canceled out since it represents the first moment of mass about the center of mass, and is therefore by definition null.

In the latter case [4.37] can be expressed as the sum of the forces on each part  $k$  ( $\mathbf{r}_k$  is the center of mass of the part):

$$\begin{aligned} \mathbf{f}_g &= \sum_k \left( \int_{\text{part } k} \mathbf{a}_g(\mathbf{r}_k) \, dm_k \right) \\ &= \sum_k \left( \mathbf{a}_g(\mathbf{r}_k) \int_{\text{part } k} dm_k \right) \\ &= \sum_k (\mathbf{a}_g(\mathbf{r}_k) m_k) \end{aligned} \quad (4.41)$$

This variant is more intensive from a computational cost standpoint, but it can be more precise for very extended bodies, over which the gravity gradient can't be assumed to be constant and the linear field approximation is unacceptably imprecise.

### Torque

The torque due to gravity on an extended body about its center of mass is calculated as follows:

$$\mathbf{T}_g = \int_{S/C} \Delta \mathbf{r} \times \mathbf{a}_g(\mathbf{r}) dm \quad (4.42)$$

Where  $\Delta \mathbf{r}$  is defined as in [4.38]. Again, the spacecraft can either be considered as an extended body characterized by mass and moment of inertia, or as a collection of point masses, one for each part.

In the former case the same linear approximation of the local gravitational field as in [4.39] is assumed. Equation [4.42] can therefore be expressed as follows:

$$\begin{aligned} \mathbf{T}_g &= \int_{S/C} \Delta \mathbf{r} \times [\mathbf{a}_g(\mathbf{r}_0) + \mathbf{G}_g(\mathbf{r}_0)] \Delta \mathbf{r} dm \\ &= \int_{S/C} \Delta \mathbf{r} \overset{0}{\times} \mathbf{a}_g(\mathbf{r}_0) dm + \int_{S/C} \Delta \mathbf{r} \times \mathbf{G}_g(\mathbf{r}_0) \Delta \mathbf{r} dm \\ &= \int_{S/C} \Delta \mathbf{r} \times \mathbf{G}_g(\mathbf{r}_0) dm \end{aligned} \quad (4.43)$$

The first integral is again the first moment of mass and can be canceled. The second integral involves the moment of inertia, however it can't immediately be expressed in a simple equation. A solution is found in [9], and is as follows:

$$\mathbf{T}_g = \begin{bmatrix} G_{yz}(I_{zz} - I_{yy}) & +G_{xz}I_{xy} & -G_{xy}I_{xz} & +I_{yz}(G_{zz} - G_{yy}) \\ G_{xz}(I_{xx} - I_{zz}) & +G_{xy}I_{yz} & -G_{yz}I_{xy} & +I_{xz}(G_{xx} - G_{zz}) \\ G_{xy}(I_{yy} - I_{xx}) & +G_{yz}I_{xz} & -G_{xz}I_{yz} & +I_{xy}(G_{yy} - G_{xx}) \end{bmatrix} \quad (4.44)$$

In which  $I_{ij}$  and  $G_{ij}$  are the components of, respectively,  $\mathbf{G}_g(\mathbf{r}_0)$  and the mass inertia tensor of the body  $\mathbf{I}_m$ .

In the latter case [4.42] can be expressed as the sum of the torques generated by the forces on each part  $k$  ( $\mathbf{r}_k$  is the center of mass of the part):

$$\begin{aligned} \mathbf{T}_g &= \sum_k \left( \int_{\text{part } k} \Delta \mathbf{r}_k \times \mathbf{a}_g(\mathbf{r}_k) dm_k \right) \\ &= \sum_k \left( \Delta \mathbf{r}_k \times \mathbf{a}_g(\mathbf{r}_k) \int_{\text{part } k} dm_k \right) \\ &= \sum_k (\Delta \mathbf{r}_k \times \mathbf{a}_g(\mathbf{r}_k) m_k) \end{aligned} \quad (4.45)$$

A more precise (but computationally costly) alternative to these two methods would be to apply the former to each individual part, and then to sum forces and torques over the whole spacecraft. At this time, however, this alternative is not implemented in AMOSPy.

## 4.5 SRP forces modeling

A generic surface stricken by EM radiation can be roughly characterized by 4 coefficients, indicating which fraction of the radiation will be reflected, absorbed or transmitted:

- $C_t$  for the transmitted fraction
- $C_a$  for the absorbed fraction
- $C_{rd}$  for the diffusively reflected fraction
- $C_{rs}$  for the specularly reflected fraction

The sum of this 4 coefficients must be equal to unity, therefore actually only 3 (the last 3 in the case of **AMOSPy**) are required to determine the surface properties:

$$C_t + C_a + C_{rd} + C_{rp} = 1 \quad (4.46)$$

EM radiation carries moment. Given a certain energy flux  $\Phi$ , the pressure generated by a complete absorption is given by  $\Phi/c$ . For instance, since the solar constant at 1 AU is  $\approx 1350 \text{ W/m}^2$ , the solar radiation pressure (SRP) in the proximity of the Earth is  $\approx 4.5 \mu\text{Pa}$ .

### 4.5.1 Force components on an illuminated surface

In order to compute the SRP force on an elementary planar surface it is necessary to sum the force components due to the various fractions of light.

An area  $dA$ , with normal versor  $\hat{\mathbf{n}}$  is stricken by a ray incoming at an angle  $\theta$  with said normal. The versor  $\hat{\mathbf{s}}$  points to the *origin* of the ray (i.e. it is opposite to the ray itself). The incident momentum flux will be  $\Phi/c \, dA \cos \theta$ .

The objective is to calculate the total force  $d\mathbf{f}_p$  due to radiation pressure [15].

#### Specularly reflected component

The momentum of the specularly reflected component is due to two contributions: the incident ray and the re-emitted ray (Figure 4.9). Both rays have the same intensity and form the same angle with the surface normal, thus the resultant will be directed along the normal versor (in the opposite direction) and only due to the perpendicular component of the ray.

$$d\mathbf{f}_{ps} = -\frac{\Phi}{c} dA \cos \theta (2C_{rs} \cos \theta \hat{\mathbf{n}}) \quad (4.47)$$

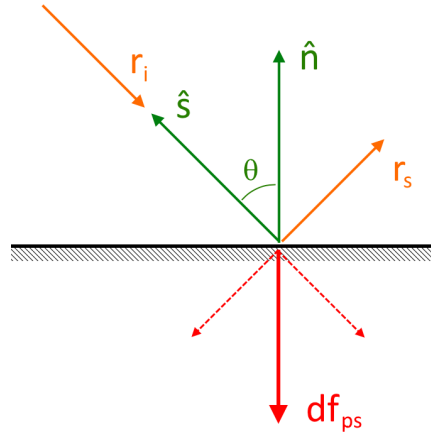


Figure 4.9: Force diagram for specularly reflected component

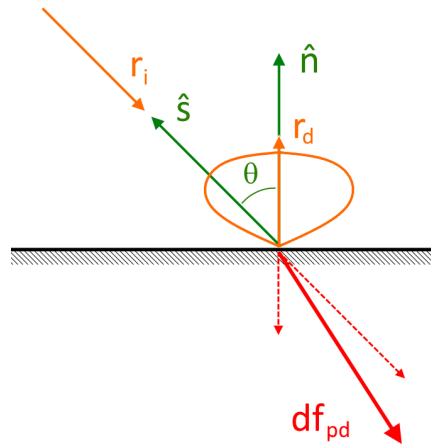


Figure 4.10: Force diagram for diffusively reflected component

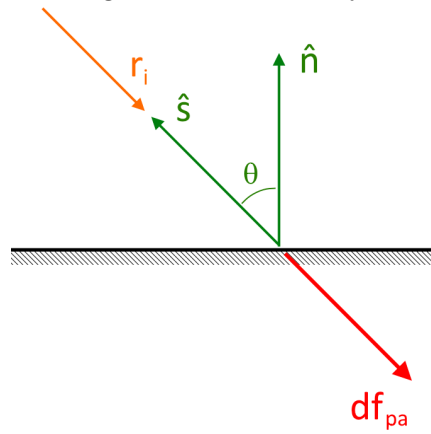


Figure 4.11: Force diagram for absorbed radiation component

### Diffusively reflected component

The momentum of the diffusively reflected component is due to two contributions: the incident ray and the re-emitted rays (Figure 4.10). The re-emitted rays are symmetrically distributed around the normal vector, and their resultant momentum is 2/3 that of the incident ray [15].

$$d\mathbf{f}_{pd} = -\frac{\Phi}{c} dA \cos \theta \left( C_{rd} \hat{\mathbf{s}} + \frac{2}{3} C_{rd} \hat{\mathbf{n}} \right) \quad (4.48)$$

### Absorbed component

The momentum of the absorbed component is completely transferred to the surface (Figure 4.11), therefore this force component can be written as:

$$d\mathbf{f}_{pa} = -\frac{\Phi}{c} dA \cos \theta (C_a \hat{\mathbf{s}}) \quad (4.49)$$

### Resultant force

The total force on the surface element can therefore now be obtained by summing these 3 contributions:

$$\begin{aligned} d\mathbf{f}_p &= d\mathbf{f}_{ps} + d\mathbf{f}_{pd} + d\mathbf{f}_{pa} \\ &= -\frac{\Phi}{c} dA \cos \theta \left[ \left( 2C_{rs} \cos \theta + \frac{2}{3} C_{rd} \right) \hat{\mathbf{n}} + (C_{rd} + C_a) \hat{\mathbf{s}} \right] \end{aligned} \quad (4.50)$$

## 4.5.2 Computation of SRP forces and torques

In order to obtain the net force on the spacecraft, equation [4.50] should be integrated over the whole surface, and then again used in another integral to calculate torque:

$$\mathbf{f}_p = \int_{\text{surface}} d\mathbf{f}_p \quad (4.51)$$

$$\mathbf{T}_p = \int_{\text{surface}} \Delta \mathbf{r} \times d\mathbf{f}_p \quad (4.52)$$

In which  $\Delta \mathbf{r}$  is defined as in [4.38] as the position of a given point wrt. the spacecraft center of mass.

### Cannonball model

Closed, analytical solutions to the [4.52] do indeed exist for some convex spacecraft geometries. One example is the cannonball model, which approximates the spacecraft

with a sphere. The result of this model is very simple:

$$\mathbf{f}_p = -\frac{\Phi}{c}\pi R^2 \left( C_{rs} + \frac{13}{9}C_{rd} + C_a \right) \hat{\mathbf{s}} \quad (4.53)$$

$$\mathbf{T}_p = 0 \quad (4.54)$$

This formulation, however, is overly simplified and often unsuitable to model certain phenomena. For instance, no torque can be modeled with this approach, while in some cases torque might indeed be the primary concern of a SRP analysis.

### Forward ray-casting model

A more flexible SRP model, assuming that an accurate enough spacecraft geometry model is available, employs forward ray-casting. Ray-casting is a technique widely used in computer graphics, which relies on generating a large number of light "rays" (e.g. one per pixel) and computing their interception or reflection by objects in a scene in order to generate an image of said scene.

The same can be applied to SRP modeling, by casting a dense array of parallel rays originating from the Sun, large enough to completely "illuminate" the spacecraft, and then calculate for each ray its eventual impact point on the spacecraft, and the elementary force locally generated by this interaction; the integrals of [4.52] are thus transformed in a sum over the set of rays.

If the rays are picked randomly it's basically a Monte Carlo method which samples light-spacecraft interaction.

While this method can work very well for compact spacecrafts, geometries such as the E-Glider, with its thin, long appendages constitute a problem, for two reasons:

- The array of incoming rays must be wide enough to "illuminate" the whole spacecraft, whatever the spacecraft attitude might be: for instance, if the rays are generated randomly on a disc perpendicular to the Sun-spacecraft direction, the disc radius must be at least as large as the largest spacecraft dimension, which in the case of the E-Glider can be several meters. However, only a tiny fraction of incoming rays will actually strike the spacecraft, since the E-Glider electrodes can be very long but also very thin. Therefore, in order to ensure than a statistically significant number of rays will be cast on the spacecraft, an extremely large number of rays must be generated and analyzed in the first place, even though the vast majority won't be useful for the calculation.
- If the rays are not picked randomly, but over a regular grid (perhaps to reduce computational load), the issue of aliasing may arise: a thin, long feature (such as an electrode) might align with the grid and be right between two rows of rays, and never be illuminated, or conversely be exactly aligned with a row and get oversampled wrt. other equal surfaces. This wouldn't constitute a big issue if the



total area of the feature was small if compared to the total spacecraft surface, but for the E-Glider case a 10 m, 1 mm diameter wire has the same projected area as a  $10 \times 10$  cm CubeSat U face. Moreover, being far from the center of mass, its contribution to torque can be very significant.

It is therefore necessary to have very precise force computations even on these thin features, and forward ray-casting can't easily provide this kind of performance, not without excessive computational costs.

### Backwards ray-casting model

An alternative ray-casting model overturns the perspective by generating the rays directly on the surface, and then propagating them backwards to check for intersections and shadowing.

The spacecraft surface is approximated with a large number of small plane "facets", and a ray is generated on each one; the integrals of [4.52] are then transformed in a sum over all these elementary areas.

As for shadowing effects, a preliminary check can discard those facets which are certainly in shadow (if  $\hat{\mathbf{s}} \cdot \hat{\mathbf{n}} < 1$ , i.e. the ray comes from behind the surface), while the ray-casting intersection algorithms filter out the contributions from rays which would have been blocked by other surfaces (cfr. Figure 4.12)

This ensures an arbitrary degree of precision (the number of facets can simply be increased), while guaranteeing that all surfaces are represented and sampled equally. Aliasing and related phenomena can still occur (e.g. a thin feature might not be intersected by many "glancing" rays, however these errors are usually very minor (the shadow of a thin wire is hardly significant, unless it is perfectly aligned with another thin wire, in which case the ray-casting would detect it)).

### 4.5.3 Implementation in the code

AMOSPy implements the backwards ray-casting model. Efficient ray-intersection algorithms are provided for each available part geometry (cylinder, cuboid, plate and sphere) and allow for a relatively quick computation.

While certainly possible for slow enough dynamics, it is generally still impractical to perform these computations in real-time in every scenario without a significant loss of precision.

Fortunately SRP external influences are limited to the solar energy flux, which can be applied as a multiplier *a posteriori*, and whether the spacecraft is in sunlight or shadowed by the main body.

Therefore forces and torques can all be precalculated in a number of points over a map of possible attitudes, and then interpolated as necessary during the real-time integration and corrected with the actual local solar flux.

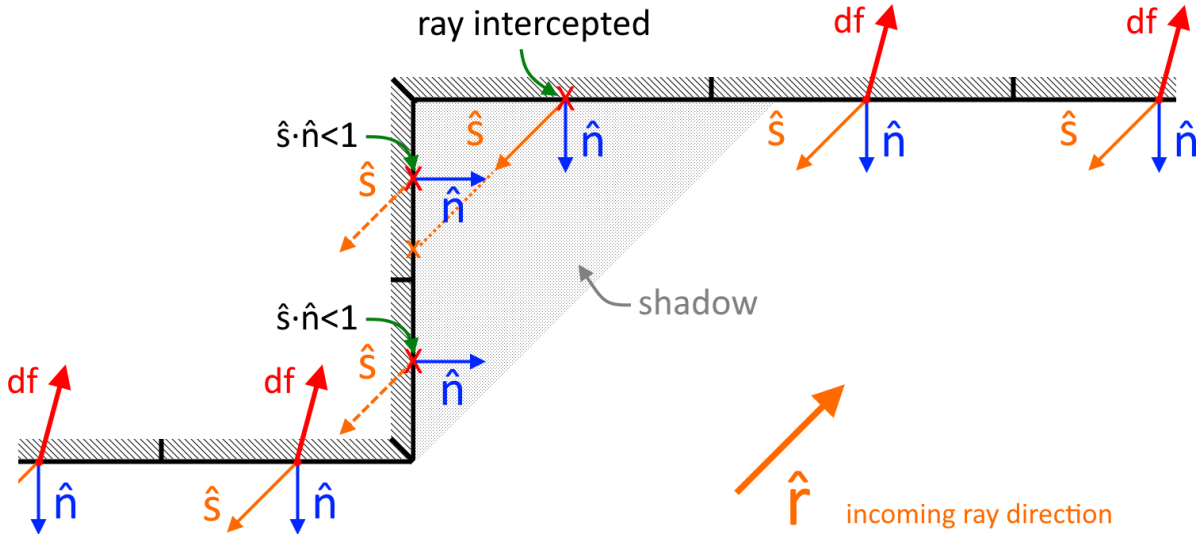


Figure 4.12: Depiction of ray-casting in AMOSPy. Some facets' contributions are discarded due to shadowing, the other components are summed over the whole surface to calculate net force and torque

AMOSPy performs this computationally costly sampling and force/torque/attitude map generation only once, when a spacecraft file is finalized, so that it doesn't need to perform it later on during the actual simulation.

## 4.6 Electrical forces modeling

Since all analytical models examined in the past have proven to be unable to adequately capture all phenomena and aspects of the plasma environment around small airless bodies, as of this day AMOSPy is only equipped to receive information on the electrostatic potential and field from external data. In defining the main body, a routine is available to read electrostatic potential and electric field data, sampled over a 3D cartesian mesh of points, from file. These files must be provided in the format used by William Yu and Dr. Joe Wang of USC for their PIC analyses (since these results will be at the base of the future investigations). The origin of the data, however, is not important: for instance, an ad-hoc preprocessor could easily compile these data files in the required format using a new analytical model.

Potential and field data are assumed to be defined in the RIC reference frame and static (i.e. time-invariant). Implementing dynamic electrostatic fields, for example taking into account the rotation of an irregular main body, represents a tough challenge with the current method, both due to the computational load and most importantly due to the quantity of data which would have to be collected beforehand (e.g. a great number of runs to map every possible asteroid-Sun attitude). This simpler approach with static fields was deemed sufficient for the time being, moreover it is already ac-

curate for the spherical test bodies which are currently under investigation (even with irregular gravity).

### 4.6.1 Forces and Torques

Whatever the electric model assumed, the simulator must be able to calculate forces and torques applied on the S/C given the local electric field  $\mathbf{E}$  and electric field gradient  $\mathbf{G}_e$ .

#### Force

Since the spacecraft is treated as an extended body, the force due to the electric field is calculated as follows:

$$\mathbf{f}_e = \int_{S/C} \mathbf{E}(\mathbf{r}) dq \quad (4.55)$$

The spacecraft can either be considered as an extended body characterized by net charge and first and second moments of charge, or as a collection of point charges localized at the center of each part.

In the former case a linear approximation of the local electric field is assumed:

$$\Delta \mathbf{r} \doteq \mathbf{r} - \mathbf{r}_0 \quad (4.56)$$

$$\mathbf{E}(\mathbf{r}) = \mathbf{E}(\mathbf{r}_0) + \mathbf{G}_e(\mathbf{r}_0) \Delta \mathbf{r} \quad (4.57)$$

In which  $\mathbf{r}_0$  is the position of the spacecraft center of mass. Equation [4.55] can then be expressed as follows:

$$\begin{aligned} \mathbf{f}_e &= \int_{S/C} [\mathbf{E}(\mathbf{r}_0) + \mathbf{G}_e(\mathbf{r}_0) \Delta \mathbf{r}] dq \\ &= \mathbf{E}(\mathbf{r}_0) \int_{S/C} dq + \mathbf{G}_e(\mathbf{r}_0) \int_{S/C} \Delta \mathbf{r} dq \\ &= \mathbf{E}(\mathbf{r}_0) q + \mathbf{G}_e(\mathbf{r}_0) \mathbf{S}_q \end{aligned} \quad (4.58)$$

The second integral cannot be canceled out as it was done with the gravitational forces, since the center of charge might not coincide with the center of mass. That term represents therefore the first moment of charge about the center of mass  $\mathbf{S}_q$ .

In the latter case [4.55] can be expressed as the sum of the forces on each part  $k$  ( $\mathbf{r}_k$  is

the center of the part):

$$\begin{aligned}
 \mathbf{f}_e &= \sum_k \left( \int_{\text{part } k} \mathbf{E}(\mathbf{r}_k) dq_k \right) \\
 &= \sum_k \left( \mathbf{E}(\mathbf{r}_k) \int_{\text{part } k} dq_k \right) \\
 &= \sum_k (\mathbf{E}(\mathbf{r}_k) q_k)
 \end{aligned} \tag{4.59}$$

This variant is more intensive from a computational cost standpoint, but it can be more precise for very extended bodies, over which the electric field gradient can't be assumed to be constant and the linear field approximation is unacceptably imprecise.

### Torque

The torque due to the electric field on an extended body about its center of mass is calculated as follows:

$$\mathbf{T}_e = \int_{S/C} \Delta \mathbf{r} \times \mathbf{E}(\mathbf{r}) dq \tag{4.60}$$

Where  $\Delta \mathbf{r}$  is defined as in [4.56]. Again, the spacecraft can either be considered as an extended body characterized by mass and moment of inertia, or as a collection of point masses, one for each part.

In the former case the same linear approximation of the local gravitational field as in [4.57] is assumed. Equation [4.60] can therefore be expressed as follows:

$$\begin{aligned}
 \mathbf{T}_e &= \int_{S/C} \Delta \mathbf{r} \times [\mathbf{E}(\mathbf{r}_0) + \mathbf{G}_e(\mathbf{r}_0)] \Delta \mathbf{r} dq \\
 &= \int_{S/C} \Delta \mathbf{r} dq \times \mathbf{E}(\mathbf{r}_0) + \int_{S/C} \Delta \mathbf{r} \times \mathbf{G}_e(\mathbf{r}_0) \Delta \mathbf{r} dq \\
 &= \mathbf{S}_q \times \mathbf{E}(\mathbf{r}_0) + \underbrace{\int_{S/C} \Delta \mathbf{r} \times \mathbf{G}_e(\mathbf{r}_0) dq}_{\mathbf{T}_{eG}}
 \end{aligned} \tag{4.61}$$

The second integral involves the second moment of charge, and can be calculated in a similar manner as for the gravity gradient torque in [??]:

$$\mathbf{T}_{eG} = \begin{bmatrix} G_{yz}(I_{zz} - I_{yy}) & +G_{xz}I_{xy} & -G_{xy}I_{xz} & +I_{yz}(G_{zz} - G_{yy}) \\ G_{xz}(I_{xx} - I_{zz}) & +G_{xy}I_{yz} & -G_{yz}I_{xy} & +I_{xz}(G_{xx} - G_{zz}) \\ G_{xy}(I_{yy} - I_{xx}) & +G_{yz}I_{xz} & -G_{xz}I_{yz} & +I_{xy}(G_{yy} - G_{xx}) \end{bmatrix} \tag{4.62}$$

In which  $I_{ij}$  and  $G_{ij}$  are the components of, respectively,  $\mathbf{G}_e(\mathbf{r}_0)$  and the second moment of charge of the body  $\mathbf{I}_q$  (it is calculated in much the same way as the inertia tensor, with charge instead of mass).

In the latter case [4.60] can be expressed as the sum of the torques generated by the forces on each part  $k$  ( $\mathbf{r}_k$  is the center of mass of the part):

$$\begin{aligned}
 \mathbf{T}_e &= \sum_k \left( \int_{\text{part } k} \Delta \mathbf{r}_k \times \mathbf{E}(\mathbf{r}_k) dq_k \right) \\
 &= \sum_k \left( \Delta \mathbf{r}_k \times \mathbf{E}(\mathbf{r}_k) \int_{\text{part } k} dq_k \right) \\
 &= \sum_k (\Delta \mathbf{r}_k \times \mathbf{E}(\mathbf{r}_k) q_k)
 \end{aligned} \tag{4.63}$$

A more precise (but computationally costly) alternative to these two methods would be to apply the former to each individual part, and then to sum forces and torques over the whole spacecraft. At this time, however, this alternative is not implemented in AMOSPy.

## 4.7 Testing and Future work

AMOSPy has recently undergone its preliminary integration testing phase, to make sure that all the modules are integrated correctly and produce sensible outputs, and that the performance is satisfactory.

Some analytical results have been compared to previous analyses and have been found to be in very good matching, with relative errors well below 1‰ (Figure 4.13, Figure 4.14).

Future work will include more extensive testing and validation, the definition of an operational set of main bodies and test spacecrafts, with other PIC-derived plasma field data, and finally the implementation and testing of charge control laws and algorithms.

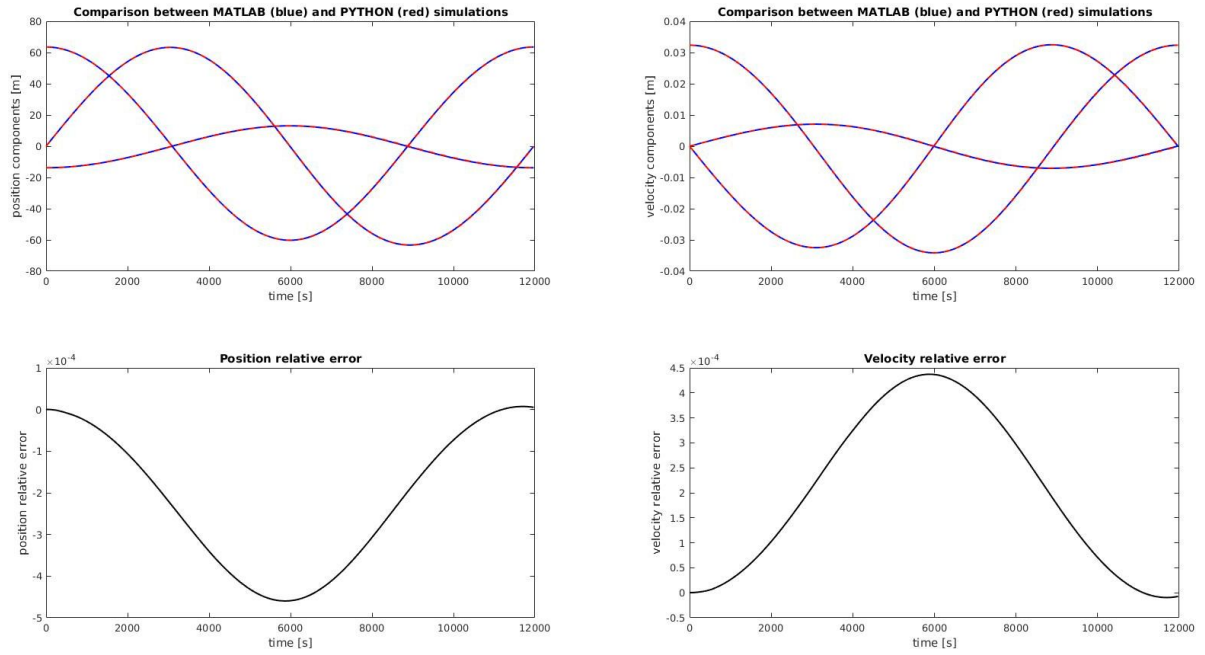


Figure 4.13: Comparison of MATLAB results (previous analyses, blue) and AMOSPy results (red) for a particular run. The results are almost perfectly overlapping. The relative errors (shown in the two lower graphs) are well within  $10^{-3}$ .

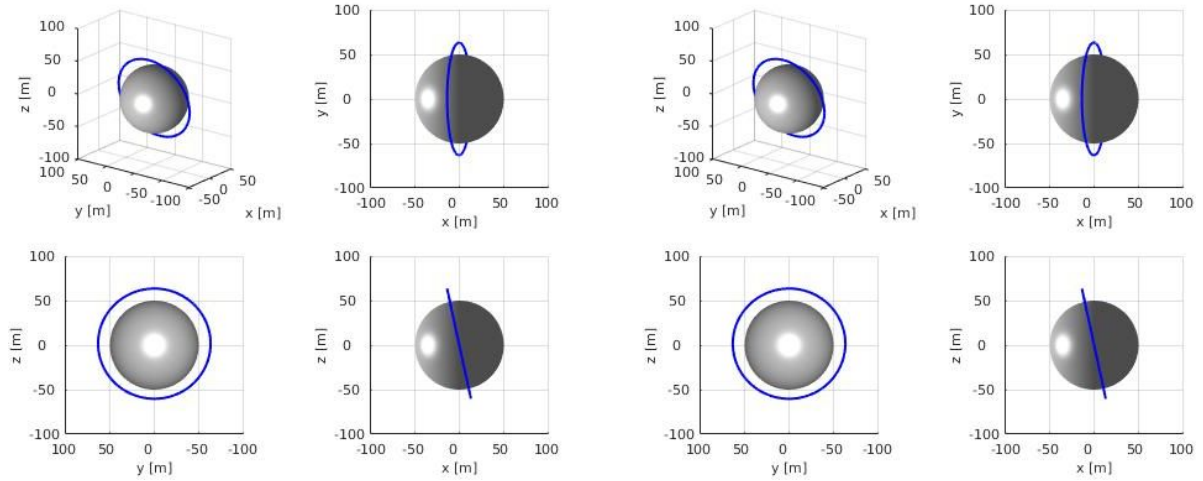


Figure 4.14: Comparison of MATLAB (previous analyses, left) and AMOSPy (right) trajectory output for the same run as the figure above.

# Chapter 5

## Conclusions

The purpose of this work was to both improve the existing models and to develop new models and simulation tools to study the E-Glider dynamics.

Three main areas of work were identified:

- The refinement and expansion of models concerning the plasma physics and electrostatics of the E-Glider interaction with the electric environment.
- The development of a complete orbital and attitude dynamics simulator, valid for arbitrary spacecraft geometries and main body properties, including modeling of gravitational, radiation pressure and electrostatic interaction.
- The definition of an active position/attitude charge control strategy and its validation through simulation.

Perhaps the most important result concerning the electrostatic interactions is the greatly reduced power requirement (if compared to the previous analyses) obtained by employing thin wire electrodes, which brings the E-Glider concept into the feasibility range of power-to-weight ratio even for solar powered nanosatellites.

Elevated electrode potentials are now probably the main limiting factor for the system design, and determining more precisely the feasibility limits for these (taking into account all kinds of secondary aspects such as sputtering, secondary emission, thermionic emission, hard radiation, vacuum discharge...) will be useful in the future for determining more precisely the design constraints.

Concerning the plasma environment, another important result was the realization that simplified analytical models can't provide accurate enough data for a reliable modeling of the electrostatic interaction, therefore data derived from PIC simulations and similar approaches should be the main source for future analyses.

As for the active control dynamics, the results obtained in the simple 2D model are greatly encouraging and suggest that an extension to the full 3D model may very well be achievable. This could be a task for the future activities on the E-Glider dynamics

modeling.

This result also proves the applicability of the E-Glider technology as a precision attitude control and stationkeeping system. Should it turn out that the requirements for the use of the E-Glider technology as a main propulsion system (hovering, levitation, ...) were impractical or unfeasible, it could still easily be repurposed as a precision manoeuvring or attitude control system. Moreover, this kind of application could possibly be performed in a wider variety of environmental conditions. If the required forces/torques were limited, even the use in LEO could perhaps be feasible (e.g. as an intermediate solution between magnetorquers and reaction wheels, with modest torques and no saturation).

Lastly, the developed multifield simulator, **AMOSPy**, has all the necessary capabilities for becoming in the future a valid software testbench for E-Glider concepts, and can allow the verification of active charge control algorithms, or trajectory stabilities, or the calculation of power requirements.

Some strong points of this simulator consist in fast, nonsingular gravity models (4.4), a very accurate and robust raytracing algorithm to calculate solar radiation pressure effects (4.5), and a proximity dynamics model which is valid also for eccentric orbits of the target body (while most standard models are only valid for quasicircular orbits) (4.3.1).



# Appendix A1

## Quaternions

Quaternions are traditionally used for representing spacecraft attitudes, since they don't present the singularity issues exhibited by Euler angles in computing the angular velocity [5].

A quaternion, in the mathematical sense, can be thought as the extension of a complex number to four dimensions. Their definition was introduced by Irish mathematician William Rowan Hamilton in 1843:

$$\begin{aligned}\mathbf{q} &\doteq q_0 + iq_1 + jq_2 + kq_3 \\ i^2 &= j^2 = k^2 = ijk = -1\end{aligned}$$

When using quaternions for representing attitude, however, one can simply think of a quaternion as a vector of four components, albeit with a peculiar algebra.

A quaternion represents a rotation about an arbitrary versor. The first component (the real part of the quaternion) represents the rotation angle  $\theta$ , while the other three identify the versor  $\hat{\mathbf{u}}$ :

$$\mathbf{q} = \begin{bmatrix} q_0 \\ \mathbf{q}_{1:3} \end{bmatrix} \doteq \begin{bmatrix} \cos(\theta/2) \\ \hat{\mathbf{u}} \sin(\theta/2) \end{bmatrix} \quad (\text{A1.1})$$

The inverse quaternion represents the inverse rotation:

$$\mathbf{q}^{-1} = \begin{bmatrix} q_0 \\ -\mathbf{q}_{1:3} \end{bmatrix} \doteq \begin{bmatrix} \cos(\theta/2) \\ -\hat{\mathbf{u}} \sin(\theta/2) \end{bmatrix} \quad (\text{A1.2})$$

Suppose that  ${}^a\mathbf{q}_b$  (with inverse  ${}^b\mathbf{q}_a$ ) represents the rotation which overlaps reference frame  $b$  to reference frame  $a$ . Then, one can use this quaternion to convert vectors among these reference frames as follows:

$$\begin{bmatrix} 0 \\ {}^a\mathbf{x} \end{bmatrix} = {}^a\mathbf{q}_b \otimes \begin{bmatrix} 0 \\ {}^b\mathbf{x} \end{bmatrix} \otimes {}^b\mathbf{q}_a \quad (\text{A1.3})$$

The operator  $\otimes$  in this context represents quaternion multiplication:

$$\mathbf{p} \otimes \mathbf{q} = \begin{bmatrix} p_0 \\ \mathbf{p}_{1:3} \end{bmatrix} \otimes \begin{bmatrix} q_0 \\ \mathbf{q}_{1:3} \end{bmatrix} = \begin{bmatrix} q_0 p_0 - \mathbf{p}_{1:3} \cdot \mathbf{q}_{1:3} \\ q_0 \mathbf{p}_{1:3} + p_0 \mathbf{q}_{1:3} - \mathbf{q}_{1:3} \times \mathbf{p}_{1:3} \end{bmatrix} \quad (\text{A1.4})$$

Even with proper optimization, using quaternions for these kinds of calculation is more computationally intensive than using simple rotation matrices (in fact it is often convenient to convert the quaternion to a rotation matrix and then use that for the calculations).

It is therefore advisable to use monolithic rotation matrices whenever necessary, e.g. for static reference frame conversions, and Euler angles derived rotation matrices for all transformations which are certainly nonsingular and whose variation law is known.

However a quaternion is still the most practical choice for attitude propagation and in case of singularities.

The quaternion rates can instead be obtained from the angular velocity as follows:

$${}^a\dot{\mathbf{q}}_b = \frac{1}{2} \begin{bmatrix} 0 \\ {}^a\omega_{ba} \end{bmatrix} \otimes {}^a\mathbf{q}_b \quad (\text{A1.5})$$

As used in the second cardinal equation of motion [\[4.23\]](#)

# Appendix A2

## Fast Keplerian Solver

The Kepler problem is the calculation of the position law  $\nu(t)$  along a keplerian orbit. One can define three "anomalies" (i.e. angular positions along an orbit):

- $\nu$ , the true anomaly, defined as the angle between the periapsis and the orbiting body, centered on the parent body;
- $E$ , the eccentric anomaly, defined as the angle between the periapsis and the orbiting body, centered on the orbit center;
- $M$ , the mean anomaly, defined as the eccentric anomaly of an ideal body orbiting on a circular orbit with the same semi-major axis as the real one (and same epochs at periapsis  $t_P$ ).

Of these, the mean anomaly  $M$  has a known law  $M(t)$ , while the others are bound to each other by two equations:

$$M(t) = n(t - t_P) = \sqrt{\frac{\mu}{a^3}}(t - t_P) \quad (\text{A2.1})$$

$$E(t) = M(t) + e \sin E(t) \quad (\text{A2.2})$$

$$\nu(t) = \arccos\left(\frac{e - \cos E(t)}{e \cos E(t) - 1}\right) \quad (\text{A2.3})$$

Of these, equation [A2.2] is transcendental, therefore it must be solved numerically.

### Initial value

Equation [A2.2] itself can be used as an iterative method:

$$E_{k+1} = M + e \sin E_k \quad (\text{A2.4})$$

Assuming  $E_0 = M$ , which is the limit in the case  $e \rightarrow 0$ , one can write an explicit third order approximation as follows:

$$E_i = M + e \sin M + e^2 \sin M \cos M + \frac{1}{2}e^3 \sin M(3 \cos^2 M - 1) \quad (\text{A2.5})$$

### Convergent iteration

While the previous iteration is valid for a first, quick approximation, a more sophisticated method is then required to quickly reduce the residual error.

A residual error function  $f$  is defined:

$$f(x) \doteq x - e \sin x - M \quad (\text{A2.6})$$

Per definition,  $f(E) = 0$ . The error on the eccentricity value can be defined as  $\varepsilon \doteq x - E$ . One can then write a Taylor expansion about  $E = x - \varepsilon$  as:

$$f(x - \varepsilon) = (x - e \sin x - M) - (1 - e \cos x)\varepsilon + \frac{1}{2}(e \sin x)\varepsilon^2 - \frac{1}{6}(e \cos x)\varepsilon^3 \dots \quad (\text{A2.7})$$

In Horner form one could write:

$$\left\{ \begin{array}{l} f(x - \varepsilon) = (x - e \sin x - M) - (1 - e \cos x)\varepsilon \quad (\text{A2.8a}) \\ f(x - \varepsilon) = (x - e \sin x - M) - (1 - e \cos x - \frac{1}{2}(e \sin x)\varepsilon)\varepsilon \quad (\text{A2.8b}) \\ f(x - \varepsilon) = (x - e \sin x - M) - (1 - e \cos x - (\frac{1}{2}(e \sin x) - \frac{1}{6}(e \cos x)\varepsilon)\varepsilon)\varepsilon \quad (\text{A2.8c}) \\ \dots \end{array} \right.$$

For each equation, one can force the LHS to 0 and solve for the external  $\varepsilon$  to obtain a new iterative method of order  $n$ .

$$\left\{ \begin{array}{l} \varepsilon_{k+1} = \frac{x_k - e \sin x_k - M}{1 - e \cos x_k} \quad (\text{A2.9a}) \\ \varepsilon_{k+1} = \frac{x_k - e \sin x_k - M}{1 - e \cos x_k - \frac{1}{2}(e \sin x_k)\varepsilon_k} \quad (\text{A2.9b}) \\ \varepsilon_{k+1} = \frac{x_k - e \sin x_k - M}{1 - e \cos x_k - (\frac{1}{2}(e \sin x_k) - \frac{1}{6}(e \cos x_k)\varepsilon_k)\varepsilon_k} \quad (\text{A2.9c}) \\ \dots \end{array} \right.$$

Finally, one can substitute the  $\varepsilon_{k+1}$  from the LHS of each equation into the  $\varepsilon_k$  of the RHS of the following one, in order to build a direct iteration in the form  $\varepsilon_{k+1} = g(x_k)$  of order  $n$  (since in the first equation  $\varepsilon_k$  is not present in the RHS). This can then be used to refresh  $x$  (the eccentricity estimate):

$$x_0 \doteq E_i \text{ [A2.5]} \implies \varepsilon_{k+n} = g(x_k) \implies x_{k+n} = x_{k+n} - \varepsilon_{k+n} \dots \quad (\text{A2.10})$$

For AMOSPy the third order iteration was chosen, as it is shown in [18] that, when combined with the third order initial estimate, it constitutes the fastest algorithm of this family.

The iteration is stopped when  $\varepsilon$  becomes smaller than a certain arbitrarily imposed threshold.

## Code

A snippet of simplified code from AMOSPy, containing a computationally optimized version of the algorithm described above, is presented here:

```
def propagate(self, t, output='ni', tol=1e-12, maxiter=1e2):
    # Calculate mean anomaly
    M = self.M0 + (t-self.t0)*self.n
    M = M % (2*np.pi)
    if output.upper() in ('M',):
        return M
    # Calculate eccentric anomaly
    # 3rd order iterative method from Murison 2006
    loop = True
    iter = 0
    s = np.sin(M)
    c = np.cos(M)
    E = M + self.e*s + (self.e**2)*s*c + 0.5*(self.e**3)*s*(3*(c**2)-1)
    while loop:
        iter = iter+1
        if iter > maxiter:
            raise RuntimeError("Kepler solver failed to converge")
        x1 = np.cos(E)
        x2 = self.e*x1-1
        x3 = np.sin(E)
        x4 = self.e*x3
        x5 = x4+M-E
        x6 = x5 / (x5*x4/x2/2+x2)
        dE = x5 / ((x3/2-x1*x6/6)*x6*self.e + x2)
        if abs(dE) < tol:
            loop = False
        E = E - dE
    E = E % (2*np.pi)
    if output.upper() in ('E',):
        return E
    # Calculate true anomaly
    ni = np.arccos((self.e-np.cos(E))/(self.e*np.cos(E)-1))
    if E > np.pi:
        ni = 2*np.pi - ni
    ni = ni % (2*np.pi)
    if output.lower() in ('ni',):
        return ni
    else:
        raise ValueError("Unrecognized or unsupported output request")
```

# Bibliography

- [1] B A Archinal et alii, "Report of the IAU Working Group on Cartographic Coordinates and Rotational Elements: 2009", *Celest. Mech. Dyn. Astr.*, **109**, 2, 2011
- [2] I C Bell III et alii, "Experimental Investigation of Electron Collection by Rectangular Cuboid Probes in a High-Speed Plasma" *IEEE Transactions on Plasma Science* **45** 7, 2017
- [3] C K Birdsall, A B Langdon, "Plasma Physics via Computer Simulation", *Institute of Physics Publishing*, Bristol, 1991
- [4] E Choiniere et alii, "Measurement of Cross-Section Geometry Effects on Electron Collection to Long Probes in Mesosonic Flowing Plasmas" *39th Joint Propulsion Conference and Exhibit* Huntsville, AL, 2003
- [5] J Diebel, "Representing Attitude: Euler Angles, Unit Quaternions, and Rotation Vectors", *Stanford University*, 2006
- [6] R A Eckman et alii, "Normalization of Gravitational Acceleration Models", 2011
- [7] W M Farrell and M D Desch, "Is there a Martian atmospheric electric circuit?", *J. Geophys. Res.*, **106**, E4, 2001
- [8] K R P Furhop, "Theory and Experimental Evaluation of Electrodynamic Tether Systems and Related Technologies", *University of Michigan*, 2007
- [9] R G Gottlieb, "Fast Gravity, Gravity Partial, Normalized Gravity, Gravity Gradient Torque and Magnetic Field: Derivation, Code and Data", *NASA Contractor Report* 188243, 1993
- [10] G Hammett "Introduction to Plasma Physics", *Princeton University*, 2010
- [11] C M Hartzell, "Dynamics of levitating dust particles near asteroids and the Moon", *J. Geophys. Res. Planets* **118**, 2013
- [12] N Hershkowitz, "Sheaths: More complicated than you think", *Physics of Plasmas* **12**, 055502, 2005
- [13] P Lee, "Dust Levitation on Asteroids", *Icarus* **124**, 0197, 1996

## BIBLIOGRAPHY

---

- [14] J B Lundberg, "Recursion Formulas of Legendre Functions for Use with Nonsingular Geopotential Models", *J. Guidance* **11**, 1, 1988
- [15] R H Lyon, "Geosynchronous Orbit Determination Using Space Surveillance Network Observations and Improved Radiative Force Modeling", *Massachusetts Institute of Technology*, 2004
- [16] D A Mendis et alii, "On the Electrostatic Charging of the Cometary Nucleus", *The Astrophysical Journal* **249**, 1981
- [17] G J Molina-Cuberos et alii, "Ion-neutral chemistry model of the lower ionosphere of Mars", *J. Geophys. Res.*, **107**, E5, 2002
- [18] M A Murison, "A Practical Method for Solving the Kepler Equation", *U.S. Naval Observatory*, 2006
- [19] T Nitter et alii, "Levitation and dynamics of charged dust in the photoelectron sheath above surfaces in space", *J. Geophys. Res.* **103**, A4, 1998
- [20] S. Pines, "Uniform Representation of the Gravitational Potential and its Derivatives", *AIAA Journal* **11**, 11, 1973
- [21] M B Quadrelli et alii, "NIAC Phase I Final Report - E-Glider: active electrostatic flight for airless body exploration", 2017
- [22] M B Quadrelli et alii, "Active electrostatic flight for airless bodies", *IEEE Aerospace Conference Big Sky*, MT, 2017
- [23] M T Tumbo, "Paschen Breakdown in a CO<sub>2</sub> Atmosphere", *AIAA*, 2013
- [24] E C Whipple, "Potentials of surfaces in space", *Rep. Prog. Phys* **44**, 1197, 1981
- [25] <https://www.grc.nasa.gov/www/k-12/airplane/atmosmrm.html>
- [26] [https://ssd.jpl.nasa.gov/sbdb\\_query.cgi](https://ssd.jpl.nasa.gov/sbdb_query.cgi)
- [27] J Wang, W Yu, University of Southern California, Private Communication